TECHNICAL REPORT No. AMRA CR64-04/3

INVESTIGATION OF SOLIDIFICATION OF HIGH-STRENGTH STEEL CASTINGS

INTERIM REPORT

by

R. V. Barone, H. D. Brody, M. C. Flemings
Department of Metallurgy
Massachusetts Institute of Technology

Code 1

for Contract Period
dates
October 1, 1963 - September 30, 1964

Contract No. DA-19-020-AMC-5443(X)
Defense Contract Administration Services
Region, Boston

AMCMS Code No. 5025.11.842
Department of the Army Project No. 1A02440A110

U. S. ARMY MATERIALS RESEARCH AGENCY
WATERTOWN, MASSACHUSETTS 02172

MASSACHUSETTS INSTITUTE OF TECHNOLOGY
CAMBRIDGE, MASSACHUSETTS 02139

Cast Steel
Microsegregation
Solidification
Homogenization

TECHNICAL REPORT NO. AMRA CR64-04/3

INVESTIGATION OF SOLIDIFICATION OF HIGH-STRENGTH STEEL CASTINGS

INTERIM REPORT

by

R. V. Barone, H. D. Brody, M. C. Flemings
Department of Metallurgy
Massachusetts Institute of Technology

for Contract Period
dates
October 1, 1963 - September 30, 1964

Contract No. DA-19-020-AMC-5443(X)
Defense Contract Administration Services
Region, Boston

AMCMS Code No. 5025.11.842
Department of the Army Project No. 1A02440A110

U. S. ARMY MATERIALS RESEARCH AGENCY
WATERTOWN, MASSACHUSETTS 02172

MASSACHUSETTS INSTITUTE OF TECHNOLOGY
CAMBRIDGE, MASSACHUSETTS 02139

ABSTRACT

Analyses of solute distribution (microsegregation) in cast alloys are extended to iron base alloys by modifying computer programs to treat alloys in which (1) the final solidification temperature and composition is variable, and (2) substantial diffusion occurs in the solid during and after solidification.

Iron-26 per cent nickel alloy is chosen for detailed computer study. Segregation ratio in this alloy can, in theory, vary from 1.0 to 3.5 depending on the value of the parameter γ^2, ($\gamma^2 = (2\ell)^2/\theta_f$, where ℓ is one half the dendrite arm spacing, assumed platelike, and θ_f is local solidification time). In experiments performed, the actual segregation ratio was found to vary from about 1.15 to 1.28 depending on solidification conditions. These results when compared with experimental values of dendrite arm spacing and solidification time are in qualitative agreement with theory. Improved quantitative agreement is believed to depend on development of an improved dendrite model for computer calculations.

Dendrite morphology was studied in columnar "unidirectional" structures of a series of binary iron-nickel alloys and in a series of iron-nickel-carbon alloys. Low solute contents and high cooling rates result in a nearly "cellular" structure. Lower cooling rates and higher solute contents result in a more complex dendritic structure, with secondary and tertiary branching. Dendrite arm spacing in the iron-nickel alloys studied generally increases, with (a) increasing cooling rate, (b) increasing nickel content (at least in the range of 15 to 26 per cent nickel), and (c) carbon additions.

TABLE OF CONTENTS

LIST OF FIGURES

I. INTRODUCTION

During the contract period immediately preceding that for which this report is written (December 9, 1962 to September 30, 1963), research was conducted on the dendritic structure, microsegregation, and homogenization of low alloy steel[1,2]. In that work, microsegregation in structures solidified at different cooling rates was quantitatively measured and shown to be relatively insensitive to cooling rate. Dendrite morphology was examined and shown to be remarkably platelike.

Homogenization was examined analytically and experimentally. Close agreement was obtained between experiment and theory. It was shown that a low alloy steel casting solidified at moderate rate requires at least an hour at 2500°F (or much longer at lower temperatures) to achieve significant homogenization of elements other than carbon. Ahearn and Quigley[3] then showed the remarkable improvement in properties obtained from such high temperature homogenization. They showed, for example, that reduction in area is increased by up to a factor of 7 at 180,000 psi yield strength.

It was clear from the foregoing that significant microsegregation exists in cast steels, that usual homogenization treatments do not eliminate it, and that it significantly affects mechanical properties of the cast alloy. Work was therefore continued during the contract year October 1, 1963 to September 30, 1964 to obtain a more

fundamental, quantitative, picture of microsegregation in iron base alloys. The specific plan of research was (1) to make a first year's effort towards developing analyses which could be employed to predict effects of solidification variables and alloy content on microsegregation, and (2) to compare these analyses with experiment. The long range aim of the research was, and is, to develop alloys, casting techniques, and homogenization procedures to produce engineering iron base alloys with minimum microsegregation.

II. ANALYSES: MICROSEGREGATION IN IRON-NICKEL ALLOYS

A. Introduction

In this section solute redistribution in iron-nickel alloys is related to the phase diagram and to the casting parameters dendrite arm spacing and solidification time. The solidification process is idealized, for the analysis, by selection of microscopic transport conditions and a growth model which has been described in detail previously[4]. The model has been employed successfully to describe microsegregation in aluminum alloys[4-5], but the analyses have been modified for application to iron-base alloys. From the point of view of computer analysis of microsegregation, significant differences between iron-base alloys such as iron-nickel and the aluminum alloys studied earlier are:

(1) absence of significant eutectic or other phase solidifying at a single temperature and composition at the end of freezing,

(2) presence of much greater diffusion in the solid (during and after solidification) than that encountered in most aluminum alloys.

Major characteristics of the model employed in both this and the previous study are no undercooling before nucleation of solid phases, complete diffusion within the liquid over distances the order of dendrite spacings, negligible diffusion in the liquid over distances the order of the two phase region, limited diffusion in the solid

phases, and a plate-like growth geometry. By application of appropriate mass balances, macroscopic parameters such as the solidification curve (fraction solid versus temperature) and the average composition of the phases are computed. In addition, detailed analyses are made of the solute distribution within the dendrites; i.e., microsegregation.

Previously, laborious hand calculations were necessary to carry out this type of analysis for any but the simplest assumptions and for any alloy systems but those having a constant partition ratio. The availability of an I.B.M. 7094 digital computer* made it feasible to carry out these analyses for an alloy system such as iron-nickel and to account in detail for casting parameters such as diffusion in the solid phases. Computations are based on the iron-nickel phase diagram drawn in Figure 2-1. This phase diagram is compiled from the best data presently available in the literature[7].

Extent of microsegregation immediately after solidification (but before cooling to room temperature) is conveniently defined by the segregation ratio, S', at that temperature:

$$S' = \frac{C'_M}{C'_m}$$

---

* The work was carried out in part at the M.I.T. Computation Center, M.I.T., Cambridge, Massachusetts.

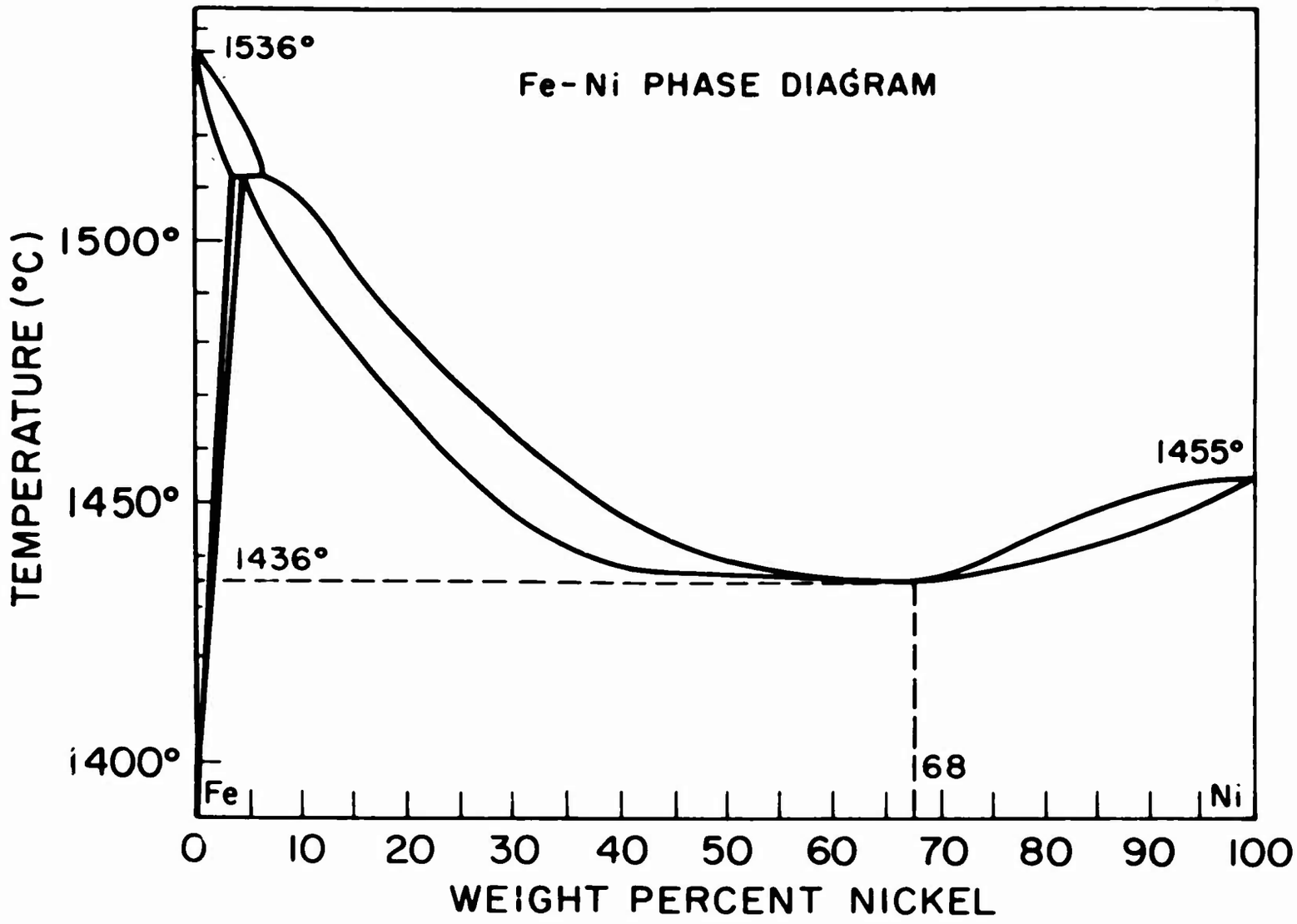

Figure 2-1: Iron-nickel phase diagrams

where: C'_M = maximum solute concentration in solid dendrite at the non-equilibrium solidus.

C'_m = minimum solute concentration in solid dendrite at the non-equilibrium solidus.

Some diffusion may occur during subsequent cooling to room temperature and so the segregation ratio, S', at room temperature will generally be less than S', and given by

$$S' = \frac{C'_M}{C'_m}$$

For the idealized plate morphology the segregation ratio S' is a single valued function of the product $\alpha k = (D_s \theta_f / \ell^2)(k)$** where D_s is the solid diffusion coefficient, θ_f is solidification time, ℓ is one half the plate spacing and k the equilibrium partition ratio. For $\alpha k << 1$, segregation ratio is a maximum; for $\alpha k >> 1$, compositions in the primary phases approach homogeneity.

B. Classical Analysis

Minimum segregation, $\alpha k >> 1$, occurs in the ideal "equilibrium" freezing; i.e., complete diffusion occurs in both solid and liquid phases, with the interface compositions as given by the phase diagram.

---

* Symbols are listed in Appendix A.

** Over the range of cooling rates that dendrite morphologies are geometrically similar and dendrite spacing is proportional to the square root of solidification time, segregation ratio is constant.

Consider an iron-26 per cent nickel alloy. The first solid forms at the liquidus temperature and is 19.3 weight per cent nickel, the alloy is completely solid at the equilibrium solidus (1456°C) and the solid is uniformly 26 weight per cent nickel. The solidification curve (temperature versus fraction solid) is drawn for an iron-26 per cent nickel alloy in Figure 2-2 and the interface composition of the solid is plotted as a function of the fraction solid in Figure 2-3.

For equilibrium solidification the segregation ratio is unity ($S' = 1$, $S^\circ = 1$). From measurements of microsegregation in slowly cooled samples[9] and unidirectionally cast ingots (Chapter V, this report), it is known that the segregation ratio in as-cast iron-26 per cent nickel alloys differs from unity and is about 1.25.

The maximum segregation ratio, for $\alpha k \ll 1$, is calculated by the classical treatment of non-equilibrium solidification[4]; i.e., complete diffusion in the liquid, no diffusion in the solid phases, and equilibrium at the interface. The solidification curve based on these assumptions is plotted in Figure 2-2. The interface composition of the solid is plotted as a function of fraction solid in Figure 2-3. Since the classical treatment allows no solid diffusion this curve represents also the final solute distribution. The alloy is not completely solid until the temperature reaches the minimum point, 1436°C. The first solid to freeze is 19.3 per cent nickel and the last solid to freeze is 68 per cent nickel. Thus, for normal non-equilibrium solidification $S' = S^\circ = 3.5$ again in poor agreement with experiment.

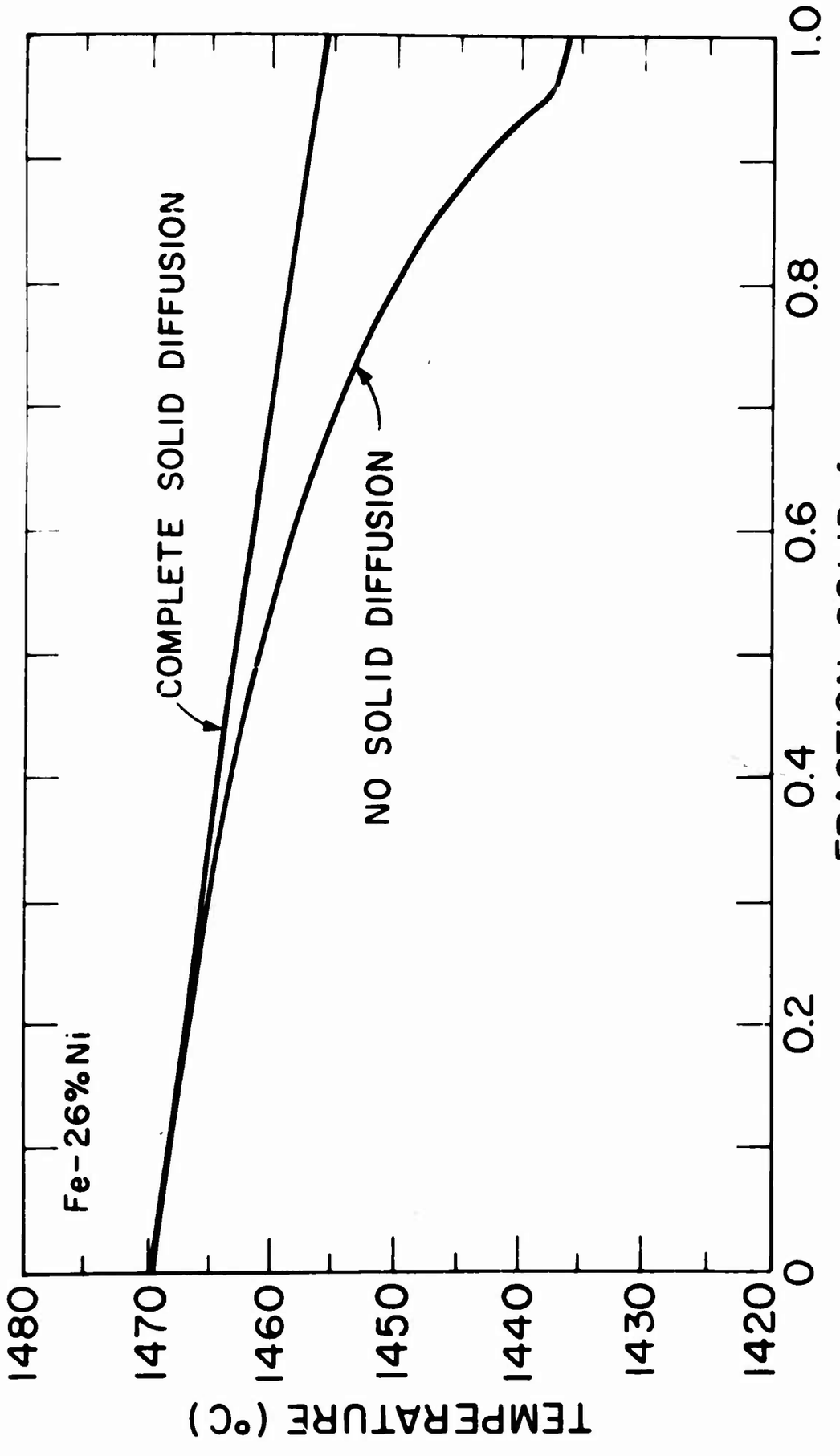

Figure 2-2: Solidification curves for iron-27 per cent nickel alloy, showing limiting cases of complete diffusion, and no solid diffusion.

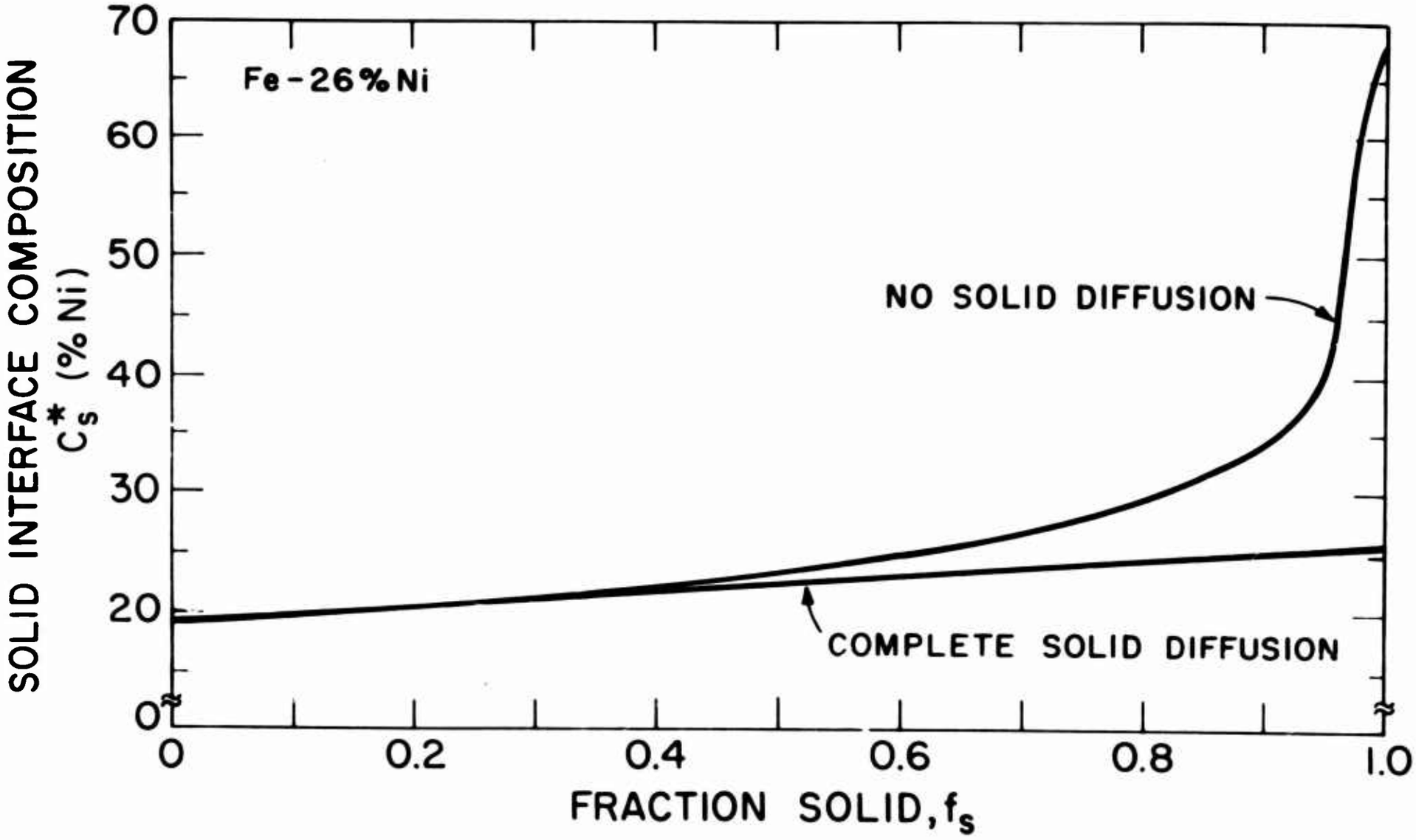

Figure 2-3: Solid composition at the liquid-solid interface, C_s^*, versus fraction solid, f_s, for limiting cases.

C. Model for Dendritic Solidification of Iron Base Alloys

It will be shown later that for iron base alloys αk is neither very large nor very small compared with 1, and diffusion in the solid must be considered in calculation of segregation ratio. (For example, for iron nickel alloys a typical value of αk is 0.1.)

Other assumptions of the classical analyses, however, remain valid. Diffusion in the liquid over distances the order of dendrite spacings is essentially complete when $D_L\theta_f/\ell^2 \gg 1$ and D_L = diffusion coefficient of solute in the liquid phase. For iron base alloys such as iron-nickel a typical value of $D_L\theta_f/\ell^2$ is 100*. The "characteristic distance**" for diffusion from the thickening dendrite arms is about 100 times the dendrite spacing.

In dendritic solidification of alloys temperature gradients provide a source of solute redistribution. As a result of the temperature gradient there is a composition gradient in the liquid increasing from the bulk composition at the dendrite tips to the liquid composition of the non-equilibrium solidus temperature at the root of the dendrites. Thus, there is a potential flux of solute across the liquid plus solid "mushy" zone and into the liquid in advance of dendrite tips.

---

* $D_s = 10^{-8}$ cm^2/sec; $\ell^2/\theta_f \sim 10^{-7}$ cm^2/sec; $k \sim 0.7$; $D_L \sim 10^{-5}$ cm^2/sec.

** The "characteristic distance" is the distance at which the solute build-up decreases to 1/e of its original value.

It has been shown previously that such a flux can be neglected[6] for $b << 1$; where b is defined:

$$b = \frac{G_L D_L}{R_t m_L} \qquad (3)$$

and G_L = temperature gradient in the liquid at the dendrite tips (°C/cm)

R_t = rate of advance of the dendrite tips (cm/sec)

m_L = slope of the liquidus line (°C/%)

For iron-nickel alloys, a typical value of b is .018*.

D. Diffusion in the Solid; Analytic Solution

A simple plate-like model, as depicted in Figure 2-4 is taken for the solidification element. The growth forms are considered to be dendrite plates separated at their centers by the final (dendrite) spacing 2ℓ. The plates start to grow smoothly at the liquidus and each face advances a distance ℓ within the solidification time θ_f.

The solute balance for an infinitesimal increment of solidification has been written in the form[4]

$$(C_L^* - C_s^*)df_s = f_s d\bar{C}_s)_{DIFF} + (1 - f_s)dC_L^* \qquad (4)$$

---

* Values used to evaluate b: $D_L = 10^{-5}$ cm^2/sec; $R_t = 10^{-2}$ cm/sec; $m_L = 2$°C/wt.%; $G_L = 35$°C/cm

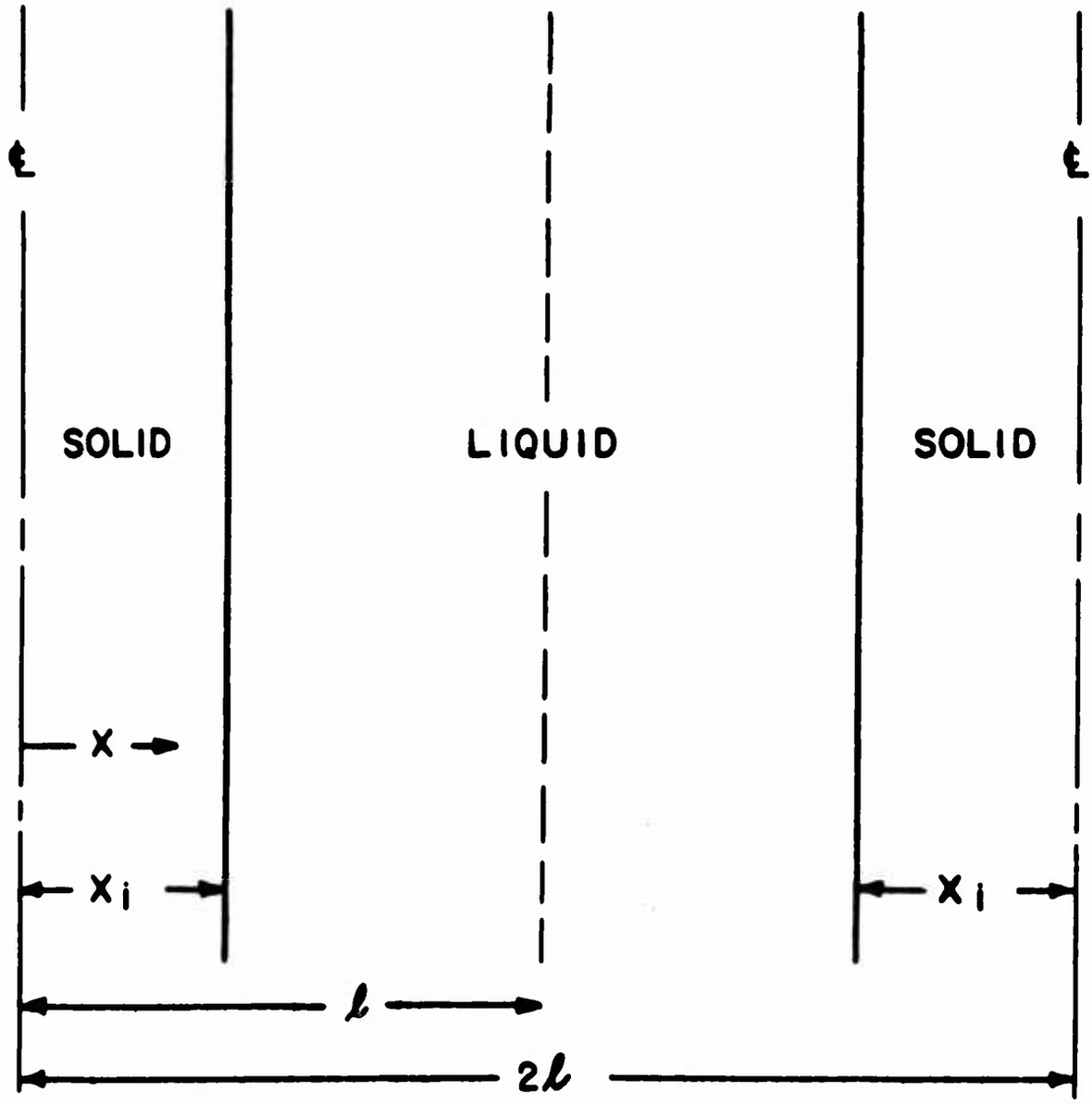

Figure 2-4: Growth model used for calculations.

$f_s d\bar{C}_s)_{DIFF}$, the solute increase in the solid due to diffusion in the solid phase, is equated to the flux entering at the interface

$$f_s d\bar{C}_s)_{DIFF} = \left(\frac{D_s}{\ell}\right)\left(\frac{dC_s}{dX}\right)_{X=X_i} d\theta \qquad (5)$$

where X_i = position of the liquid-metal interface. The concentration gradient at the interface is less than the gradient of interface composition by a factor w

$$\left(\frac{dC_s}{dX}\right)_{X=X_i} = w\,\frac{dC^*}{dX_i} \qquad (6)$$

Substituting (5) and (6) into (4)

$$(C_L^* - C_s^*)df_s = w\alpha_L dC_s^* + (1 - f_s)dC_L^* \qquad (7)$$

where

$$\alpha_L = \frac{D_s}{u\ell} \qquad (8)$$

and u = rate of growth of dendrite plate (cm/sec). An approximate analysis, one that places an upper limit on solid diffusion, has been made assuming diffusion that occurs does not change significantly the composition gradients in the solid. Then w is unity and the solidification curve or extent of microsegregation is evaluated by integration of (7).

This first approximation to solidification with diffusion was evaluated for a series of iron-nickel alloys for several values of

γ^2 where

$$\gamma^2 = \frac{(2\ell)^2}{\theta_f}$$

Results for iron-26 per cent nickel alloy are given in Figure 2-5.

Data for the diffusion coefficient used in calculations for Figure 2-5 (and subsequent work on iron-nickel alloys) are from Goldstein[10] who showed the diffusion coefficient for the γ phase varies with both temperature and nickel content according to the relation*

$$D_s = \exp\,[.0519\ X_{Ni} + 1.15]\ \exp\,\left[-\frac{38{,}380 - 5.85\ X_{Ni}}{T_k}\right] \qquad (9)$$

where X_{Ni} = mole per cent nickel

T_k = temperature, degrees Kelvin

E. Diffusion in the Solid, Finite Difference Solution

The analytic method discussed above somewhat overestimates the amount of solid diffusion during solidification (since w is assumed to be unity in equation 6). Hence the interface compositions calculated in Figure 2-5 are somewhat low. An additional limitation of the analytic method is that it does not yield a detailed description of the concentration profile within the dendrite. For example,

---

* Goldstein reports the above expression to be in agreement with his measured values of D_s within ten per cent for nickel contents up to 50% in the temperature range of 1000°C to 1288°C. In the work equation (28) is employed for compositions up to 68% nickel and in the temperature ranges 800°C to 1469.5°C.

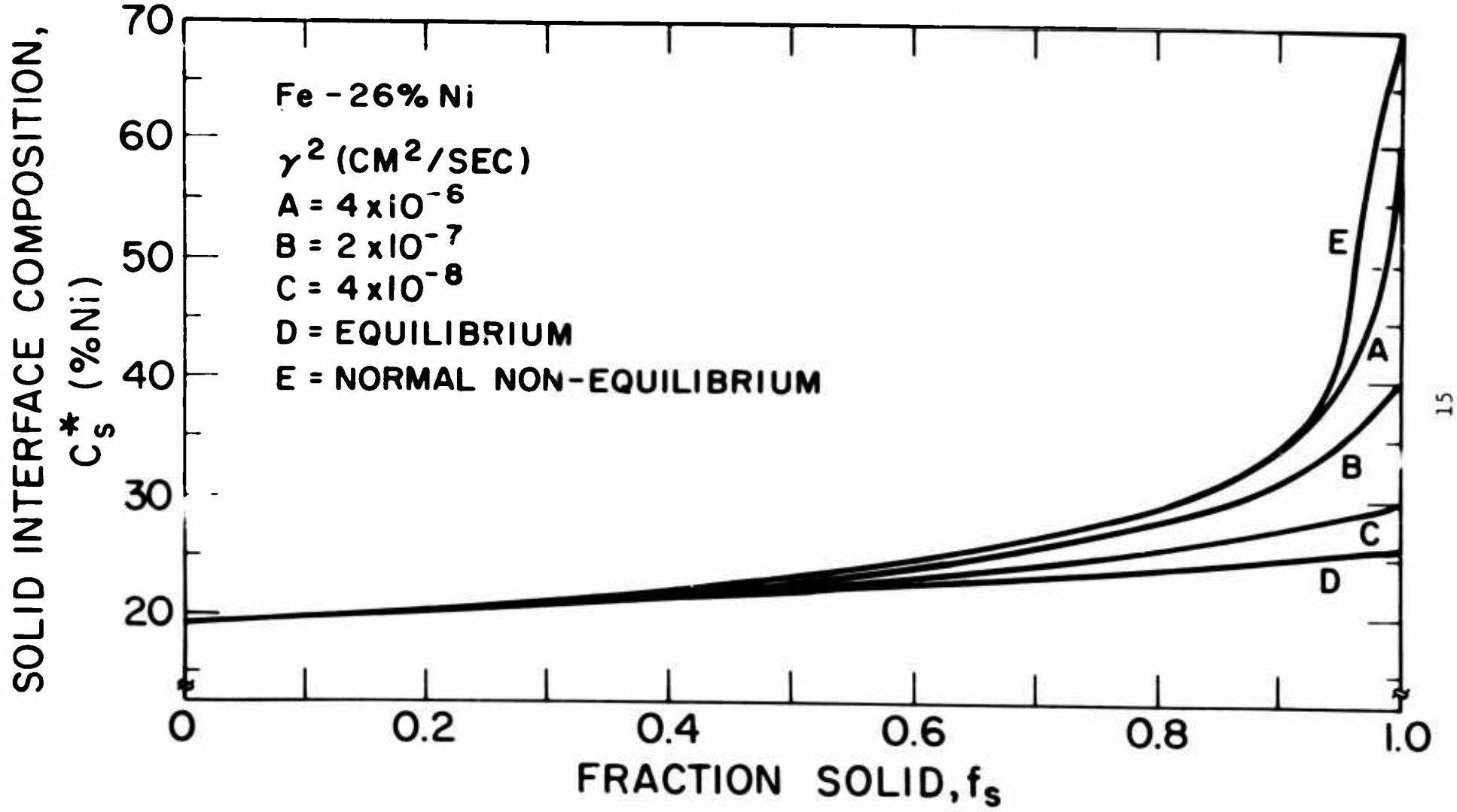

Figure 2-5: Interface composition during solidification versus fraction solid, 26-per cent nickel alloy. Results based on equation (1).

the results plotted in Figure 2-5 yield, for a given γ^2, the value of the maximum compositions at the end of freezing, (C'_M), but do not give the minimum compositions, (C'_m).

The finite difference solution to Fick's second law was therefore employed to provide more precise and detailed description. The procedure was similar to that employed previously[4] except, here, w (equation 6) was not required to be unity - this is discussed below.

The procedure employed is to solve Fick's second law

$$\frac{dC_s}{d\theta} = \frac{\partial}{\partial X}\left(D_s \frac{\partial C_s}{\partial X}\right) \qquad (10)$$

in the solidification interval using the initial and boundary conditions implied by the model, Figure 2-4. These conditions are:

$$\begin{aligned} &\text{when } T = T_L,\ \theta = 0;\ X_i = 0, \text{ and } C_s(X_i) = kC_o \\ &\text{at } X = 0,\ \frac{\partial C_s}{\partial X} = 0;\ X = X_i,\ C_s(X_i) = C_s^* \end{aligned} \qquad (11)$$

The boundary conditions of the finite difference solution during solidification require as input data the interface composition of the solid as a function of fraction solid. In previous work, the envelope of interface compositions for a particular value of γ^2 was obtained by integrating the analytic expression (equations 4 through 6) using a value of w = 1 and then using the resulting data as input to the finite difference solution for the same value of γ^2. Such a procedure was shown to be satisfactory in non-ferrous systems when

αk was sufficiently small and C_M' was fixed by an invariant transformation at the end of solidification (e.g., in eutectic formation). For ferrous alloys and specifically for the iron-nickel alloys considered here, αk is larger and the maximum solid composition is not confined to one value. For improved accuracy of results it is desirable to refine the assumption of $w = 1$.

The procedure adopted herein was to require that solute be conserved during solidification and then to combine the analytic expression and finite difference solution. This is done in the following way. The differential mass balance, equation (7) is integrated assuming an average value for w. The envelope (C_s^* versus f_s) obtained is next employed in the finite difference techniques to compute the solute distribution in the solid dendrites. A solute balance is then made to determine if solute has been lost or grained, at the correct value of $\bar{w}$, the amount of solute in the alloy after solidification will be just equal to C_o.

Values of $\bar{w}$ for several values of γ^2 were obtained as described above for the iron-26 per cent nickel alloy. The corrected envelopes of interface composition are drawn in Figure 2-6. Note by comparison with Figure 2-5 these envelopes lie somewhat above the uncorrected values. Corrected envelopes were used for all finite difference computations made for the iron-26 per cent nickel alloy.

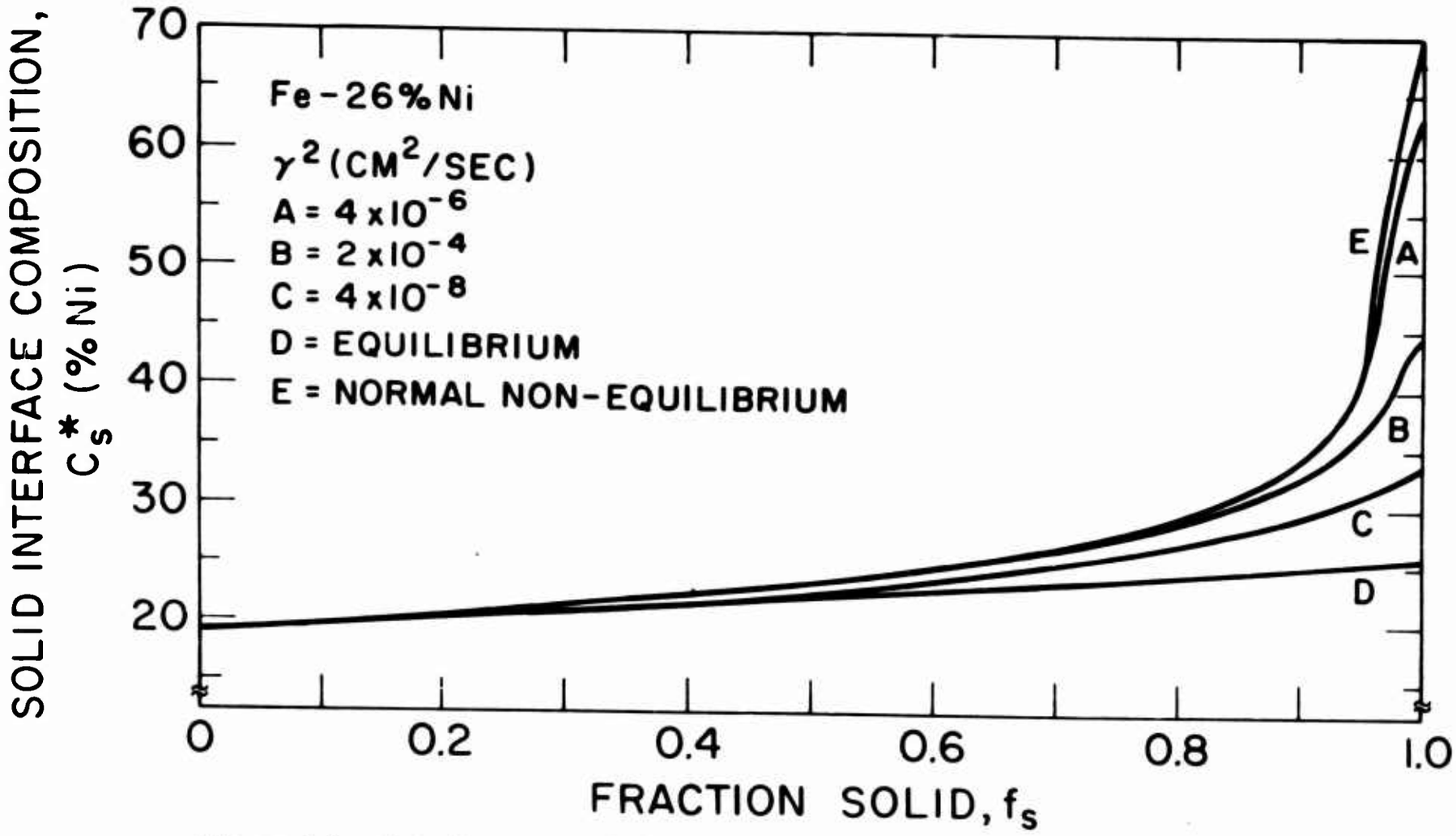

Figure 2-6: Interface composition during solidification versus fraction solid for iron-26 per cent nickel. Solute balance factor included.

Using the solute corrected envelopes, the finite difference method was used to calculate the solute distribution within an iron-26 per cent nickel alloy for several values of γ^2. In Figure 2-7, the solute distribution within an iron-26 per cent alloy is shown at several stages in solidification for a value of $\gamma^2 = 4 \times 10^{-8}$ cm^2/sec. Due to diffusion in the solid, the minimum solute content increases continuously during solidification.

The variation of the non-equilibrium solidus temperature is shown in Figure 2-8. The solidus varies from 1454°C to 1436°C depending on γ^2. Hence, the last solid to freeze varies from 26 per cent nickel to 68 per cent nickel depending on γ^2. In Figure 2-9, the maximum and minimum compositions for iron-26 per cent nickel alloy are plotted versus γ^2.

In addition, Figure 2-9 shows how these values change during cooling to room temperature. As the alloy cools from the non-equilibrium solidus to room temperature homogenization can occur, and the finite difference solution is readily extended to the computation of the amount of solid state homogenization. For the iron-nickel system, in which there is no second phase formed during solidification, the boundary conditions are

$$X = 0, \quad \frac{\partial C_s}{\partial X} = 0, \quad X = \ell, \quad \frac{\partial C_s}{\partial X} = 0 \qquad (12)$$

If heat flow conditions after solidification while solid diffusion is important are the same as during solidification, the time

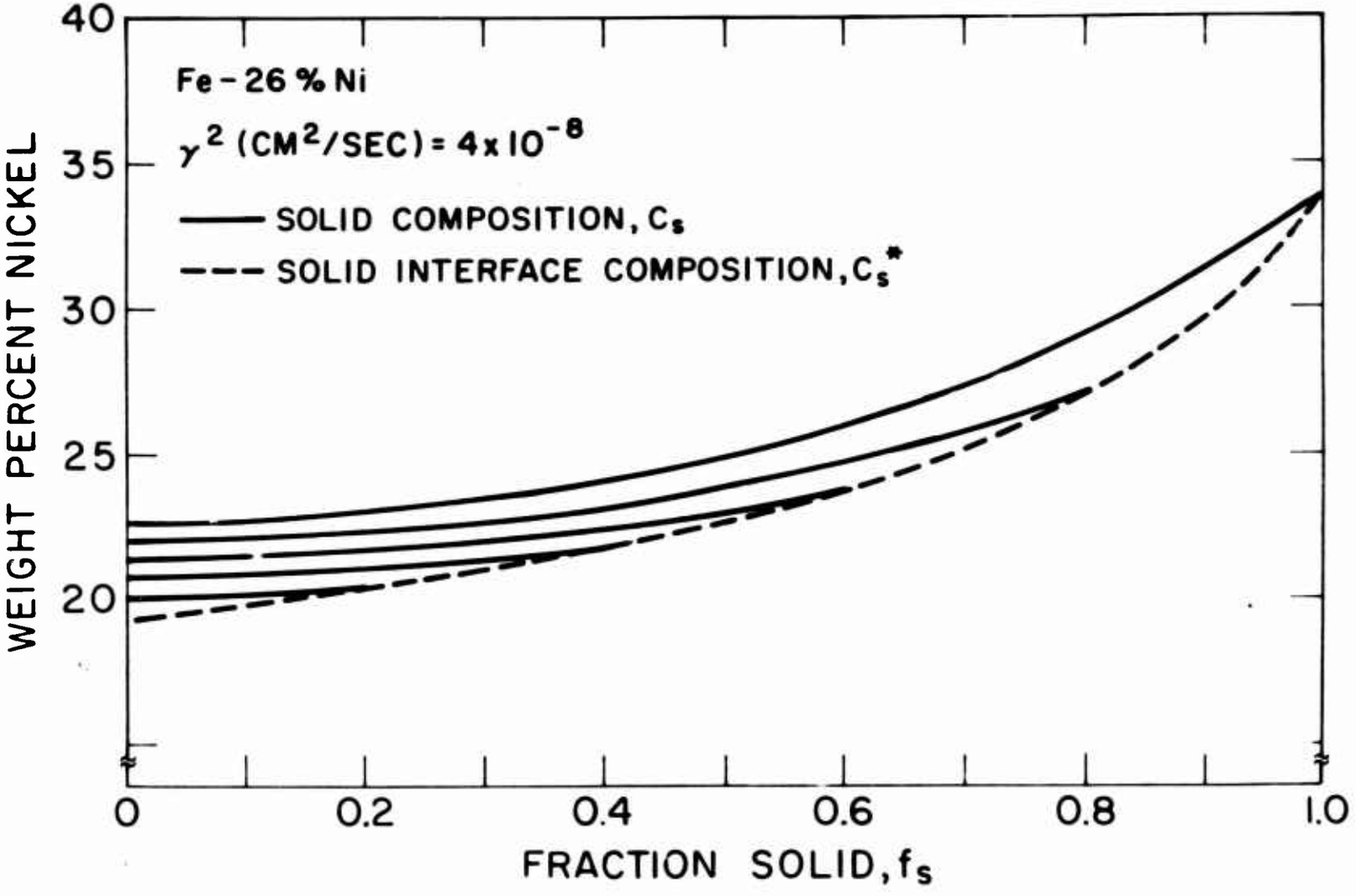

Figure 2-7: Solute composition at the interface (dashed line) and solute distribution in the solid at several stages of solidification. Iron-26 per cent nickel, solute balance factor included.

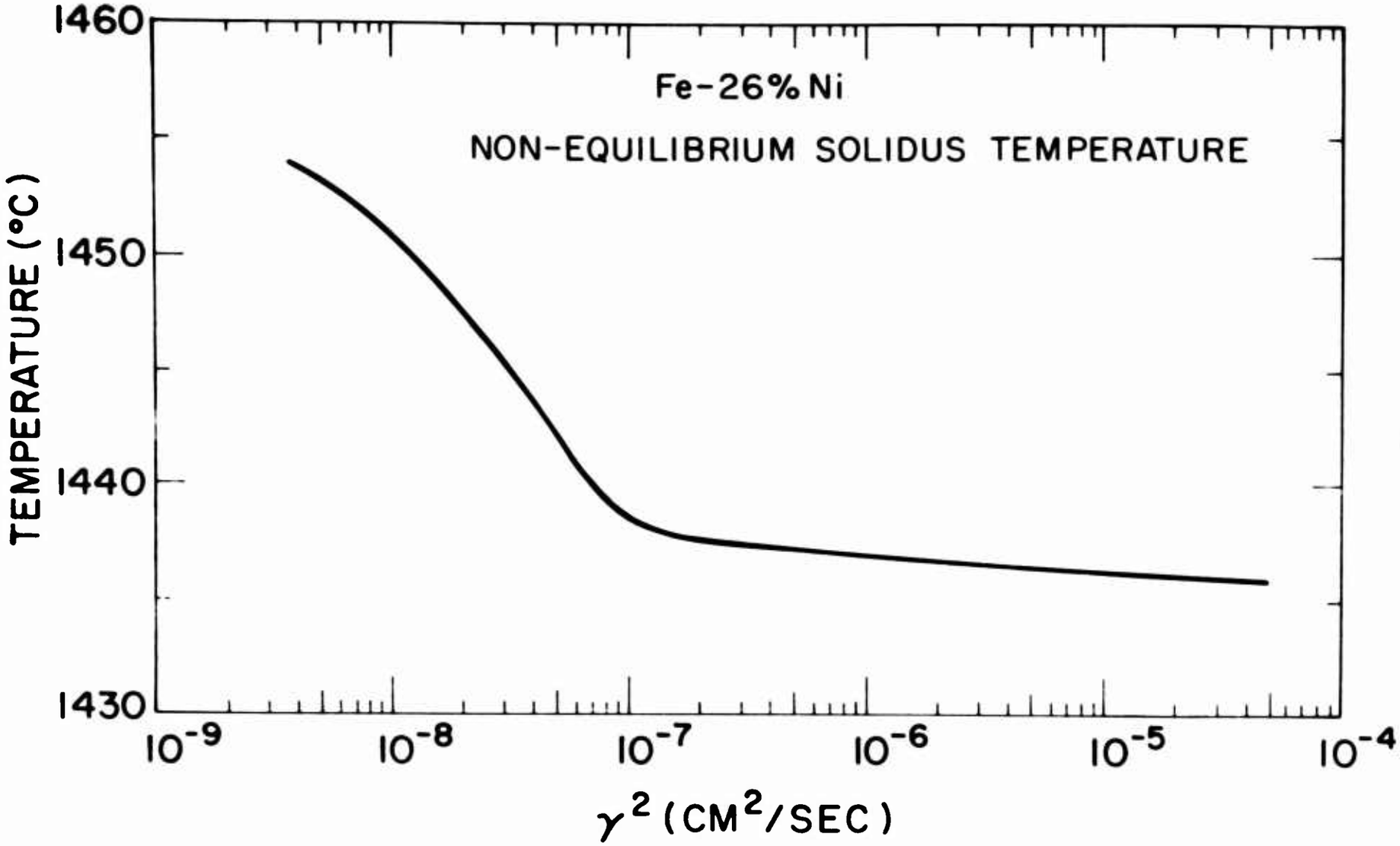

Figure 2-8: Non-equilibrium solidus temperature versus γ^2 for iron-26 per cent nickel alloy. Solute balance factor included.

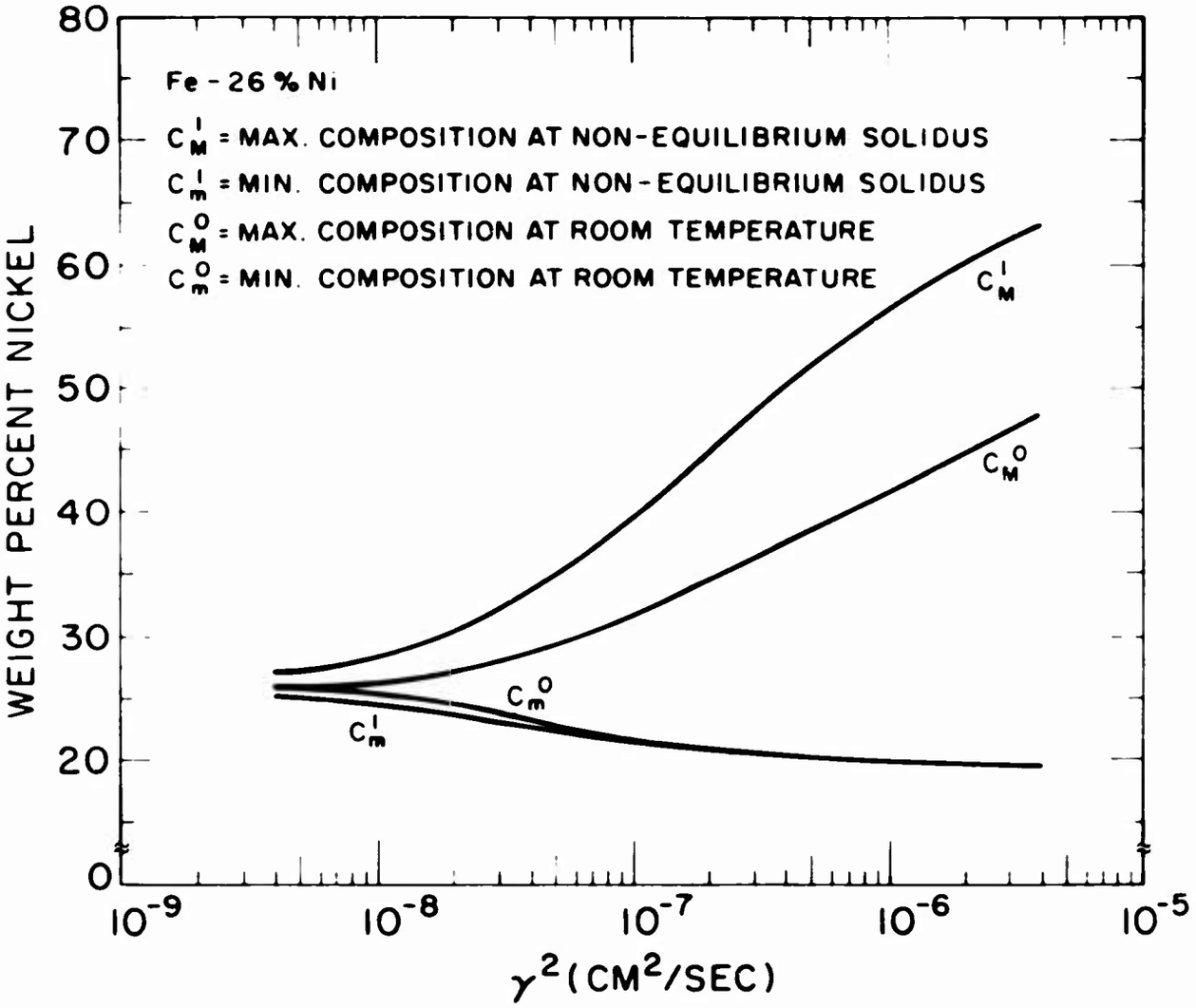

Figure 2-9: Maximum and minimum compositions at completion of solidification and at room temperature, versus γ^2.

temperature path for the alloy is given by

$$T = T'_s - \frac{H'}{C_\rho} \left(\frac{\theta - \theta_f}{\theta_f} \right) \qquad (13)$$

where T'_s = non-equilibrium solidus (°C)

H' = average heat released per unit weight of material solidified (cal/gr)

C_ρ = heat capacity of solid (cal/gr °C).

The ratio of maximum to minimum composition across a dendrite arm at the non-equilibrium solidus (S') is plotted against ^{2} in Figure 2-10. The value at room temperature (S°) is also shown. These ratios ("Segregation Ratios") vary from about 3.5 at high values of γ^2 to 1 for very low values.

In Figure 2-11 the solute distribution at the non-equilibrium solidus and at room temperature are shown for several values of γ^2. Note that diffusion in the solid after solidification has a significant effect on maximum composition, C°_M, at all values of γ^2, but little or no effect on the minimum composition.

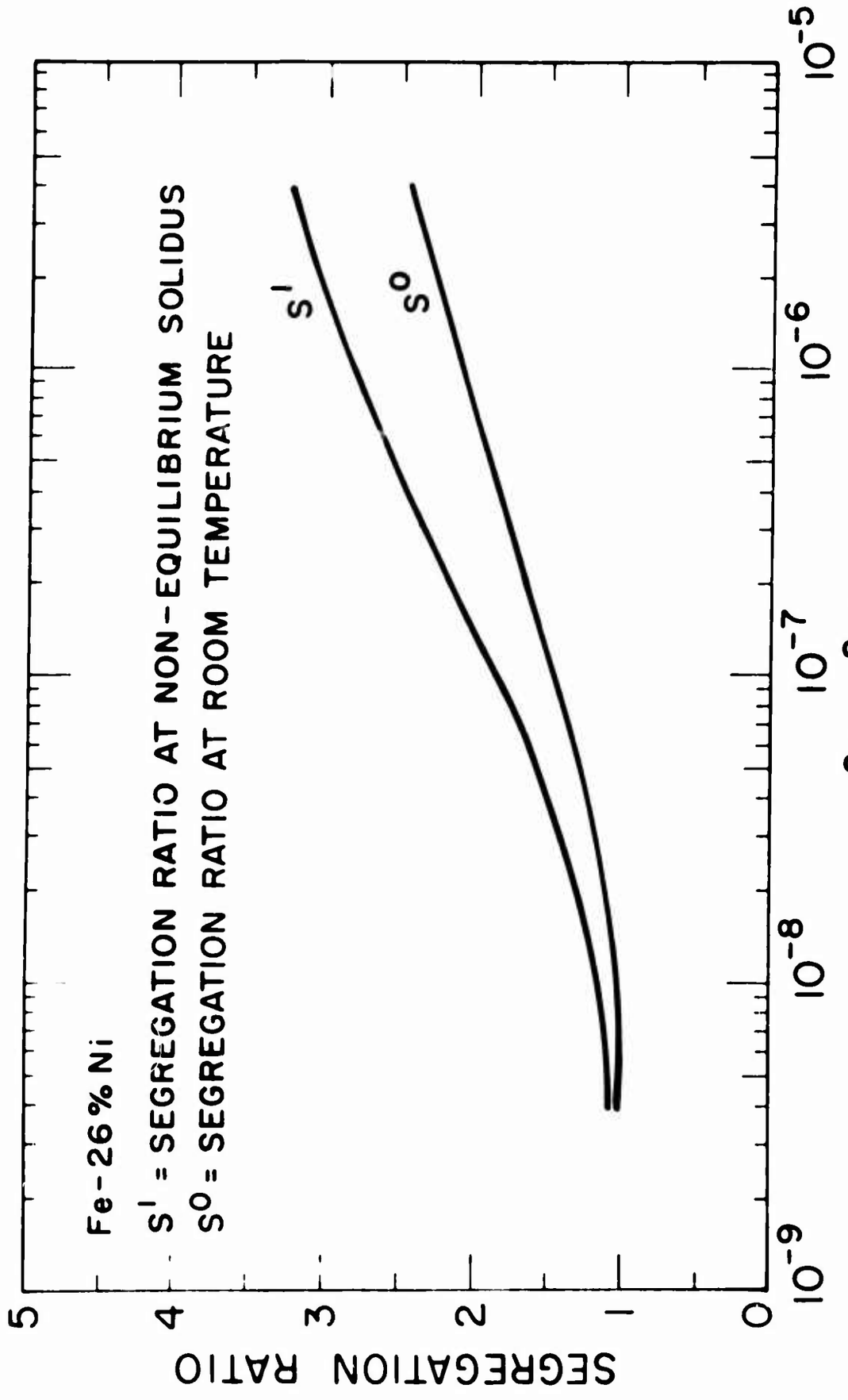

Figure 2-10: Segregati n ratio at non-equilibrium solidus and at room temperature.

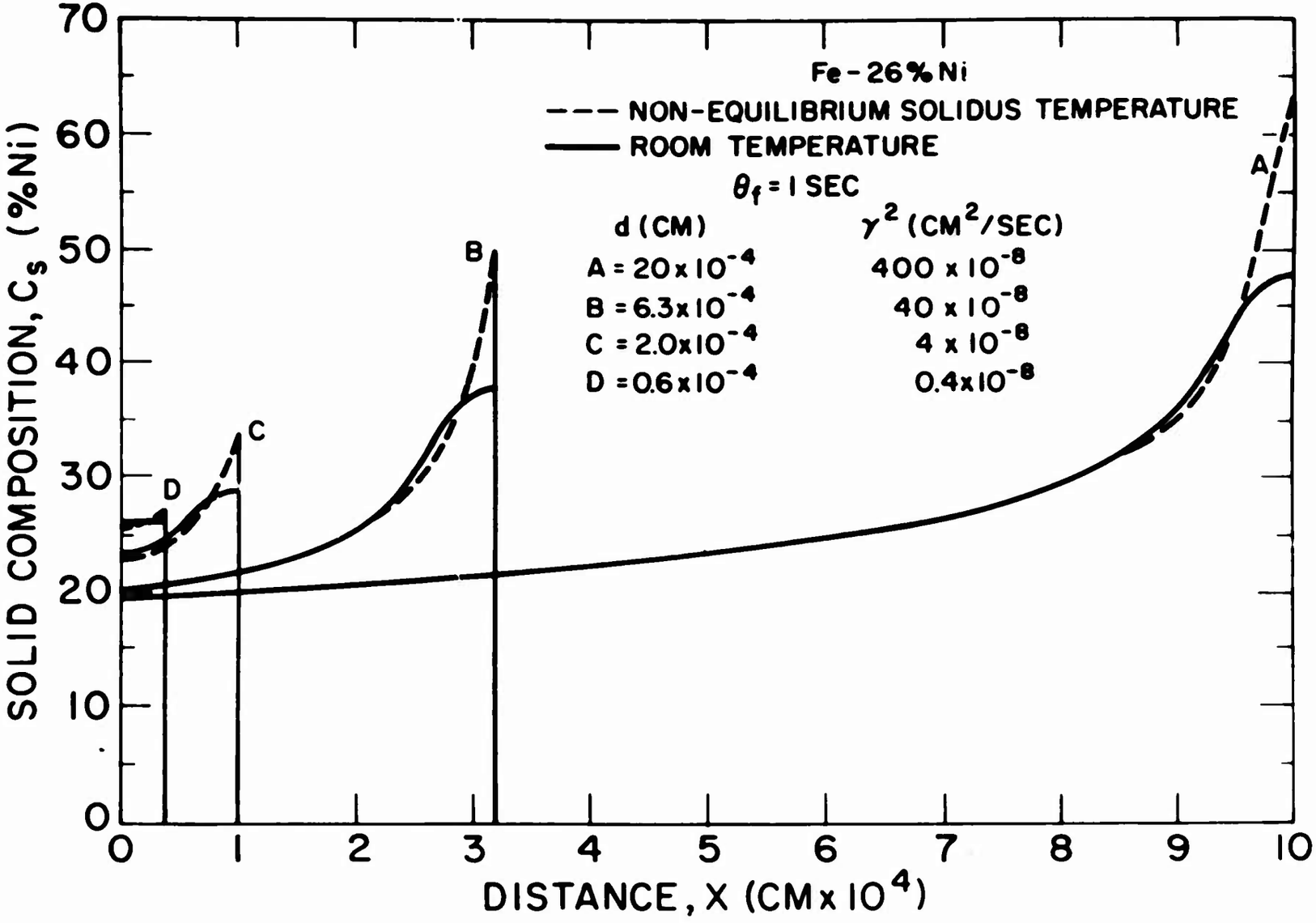

Figure 2-11: Solute distribution calculated by numerical analysis at the non-equilibrium solidus temperature and at room temperature.

III. INGOT PREPARATION

A. Alloys Investigated

A number of alloys were prepared in the iron-nickel binary system and the iron-nickel-carbon ternary system for study of microsegregation and dendrite morphology. A list of the alloys cast, the charge compositions, and the results of chemical analyses are given in Table 3-1.

B. Melting, Molding, Casting

All heats were induction melted in clay graphite crucibles with rammed linings of magnesite. Melts were deoxidized by additions of 0.5 per cent aluminum. Part or all of the aluminum was added prior to tapping at 3000°F. In all cases the temperature of the melt was measured using an optical pyrometer prior to tapping. No further temperature measurements were made before pouring.

All of the ingots were cast in plate molds 1-inch thick by 5 inches wide by 8 inches high topped by a riser which tapered from 5 inches by 1 inch to 7 inches by 3 inches over a distance of 4 inches. A schematic diagram of this mold is shown in Figure 3-1. The mold was a composite of CO_2 sand and a high temperature exothermic molding material. The exothermic sleeve was 1/2" thick at the chill and had a 5/24 in/in taper. The exothermic material ignites and heats to a temperature above that of the melting point of steel. Either of two

TABLE 3-1

Chemical Analyses of Ingots Studied

Heat Number	Nominal		Actual*		
	%Ni	%C	%Ni	%C	%Al
1	10.0	-	9.86	-	0.06
2	15.0	-	14.7	-	0.04
3	20.0	-	19.9	-	0.21
4	26.0	-	26.0	-	0.24
5	26.0	.12	25.0	0.12	0.14
6	26.0	.33	24.1	0.33	0.24
7	26.0	.42	24.6	0.42	0.18
8	26	-	25.8	-	0.47

* Chemical analyses were taken at approximately 1/2 inch from the chill. 0.5 per cent aluminum added as deoxidizer to all heats.

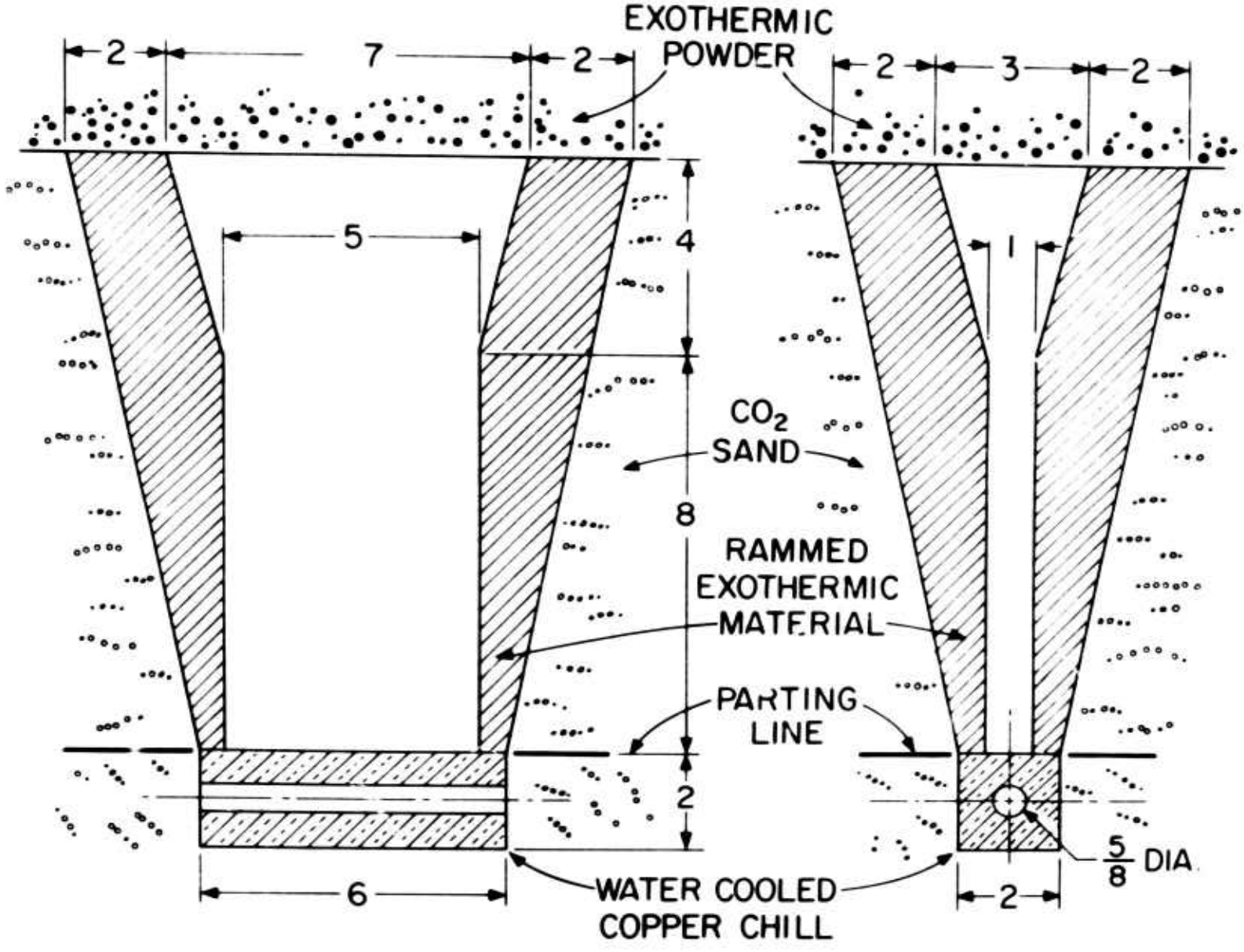

Figure 3-1: . Schematic diagram of plate mold.

commercial exothermic materials was used: Exomold E or LD Exothermic Material. To avoid gas pick-up the cope sections were all baked for a minimum of 24 hours at 600°F. The drag portion of the mold consisted of a water cooled copper chill block which was given a light zircon wash and supported by CO_2 sand.

Although the casting weighed 20 pounds, 40 pound heats were always melted in order to improve chemical and temperature control. All of the heats were skimmed, killed, tapped at 3000°F, and then top poured directly into the mold. The exothermic mold was not ignited before pouring. Hot water was first run through the chill until the molten metal was poured into the mold at which time cold water was used. This procedure prevented condensation on the chill. After filling the mold, the casting was capped with additional exothermic material to reduce top heat loss.

Structures of the castings poured were fully columnar with the columnar grains, extending from the chill up into the riser. Typical microstructures are shown in Figures 5-2 to 5-15 and are discussed in Section V.

IV. THERMAL MEASUREMENTS

A. Introduction

Polich, Nereo and Flemings[11] have estimated from heat flow analysis the rate of advance of the dendrite tips in a unidirectionally solidified ingot with an exothermic sleeve. In addition, they experimentally measured the rate of advance of an isotherm in the solid-liquid zone (a) in a plate casting having an exothermic sleeve with a 7/32 in/in taper and (b) in a plate casting having an exothermic sleeve uniformly 1-1/2 inch thick. Their results comply with the following expressions:

7/32 in/in taper $\quad X = .20 \sqrt{\theta} - 1.80 \quad$ (14a)

1-1/2 inch uniform $\quad X = .16 \sqrt{\theta} - 2.0 \quad$ (14b)

where X = position of isotherm, inches

θ = time, seconds

Their experimental results are in good agreement with estimates made from heat flow analysis.

Thermal measurements were made for a unidirectionally solidified ingot of the design employed in this investigation for the following reasons:

(1) The geometry of the exothermic sleeve used here was slightly different than that used in the previous investigations[11].

(2) A binary alloy, iron-26 per cent nickel, was used. The thermal properties of this alloy may not be much different from the 4340 alloy studies previously. However, in this instance, a reasonable value of the non-equilibrium solidus can be computed (using the equilibrium phase diagram and the computations discussed in Section II). Thus, a good estimate of the solidification time is possible.

(3) Use of a thermocouple design capable of rapid response allowed measurement of cooling curves all the way to room temperature at positions relatively close to the chill.

B. Experimental Procedure

Thermal measurements were made during the solidification and cooling of an iron-26 per cent nickel ingot (ingot No. 8) cast in a mold of the design discussed in the previous section and drawn in Figure 3-1 Twenty mil platinum-platinum-10 per cent rhodium thermocouples were inserted horizontally through the exothermic sleeve in the 5-inch direction at distances from the chill of 1 inch, 2 inches, 3 inches, 4 inches, 5 inches and 6 inches. Each thermocouple was protected by 1/16-inch i.d. and 1/8-inch i.d. fused silica tubes. In addition, a 3/16-inch fused silica protection tube was used where the thermocouple penetrated the exothermic, and a layer of CO_2 sand about 1/4 inch thick separated each thermocouple ensemble from the exothermic material. The thermocouple wire was brought out to an ice bath cold junction and connected to the recording instruments by copper lead wire. The output of the two thermocouples closest to the

chill were recorded continuously on a Moseley model 1100A two pen strip chart recorder. The remaining four thermocouples were read at thirty second intervals on a Honeywell Electronik 16 multipoint strip chart recorder. Prior to pouring of the ingot, recording channels were calibrated individually.

Inserting the thermocouples through the long horizontal direction of the plate and separating them from the exothermic material by a layer of CO_2 sand minimized both the effect of heat from the exothermic reaction on the temperature of the thermocouple junction and the effect of the thermocouple assembly on thermal conditions within the ingot. By using such thin protection tubes the volume occupied by the thermocouples was less than 4 per cent in the first six inches of the casting.

The response of the thermocouple ensemble was determined in a separate run by measuring the time for a cold thermocouple to reach the temperature of a steel bath poured around it. The thermocouple ensemble used here reached 1500°C in 8 seconds. This can be compared roughly with the thermocouple design used previously[11] which required 58 seconds to reach 1500°C in an analogous experiment.

After the run, the ingot was sectioned and the positions of the thermocouples were measured. These measured positions are used in the plots and calculations that follow. They are 1.13 inch, 2.17 inches, 3.15 inches, 4.17 inches, 5.36 inches and 6.53 inches.

C. Results of Thermal Measurements

Cooling curves measured for a unidirectionally solidified ingot are shown in Figure 4-1. The sharp change in slope of each curve indicates the time the dendrite tips reach the position of the thermocouple (due to the higher thermal conductivity of the solid). It is clear that the solidification front progresses unidirectionally from the chill. The breaks measured at thermocouples 3, 4, 5 and 6 occur at very close to the same temperature, namely 1468°C.

The position of the solidification front, X_L, identified by the thermal breaks is plotted as a function of the square root of time in Figure 4-2. Also plotted is position of the solidus, X_s (taken as liquidus minus 25°C).* Using least squares analysis, straight lines were fit to the data. The following expressions result:

$$X_L = .153 \sqrt{\theta_L} - .239 \qquad (14a)$$

$$X_s = .145 \sqrt{\theta_s} - .238 \qquad (14b)$$

with time expressed in seconds and distance in inches.

The solidification time, θ_f. as a function of distance from the chill may be derived from equations (14a) and (14b) as the difference

---

* This solidification range was predicted from Figures 2-8 and 2-10 as the difference between the liquidus and non-equilibrium solidus temperatures to yield a segregation ratio of 1.20.

between the arrival of the solidification front and the time to cool through the solidification range and reach the non-equilibrium solidus. The resulting expression is:

$$\theta_f = 4.84\ X^2 + 2.22\ X + 0.25 \qquad (14c)$$

The square root of the solidification time, θ_f, is plotted as a function of distance from the chill in Figure 4-3. Note that extrapolation of this curve to points close to the chill is not possible since here interface resistance governs heat flow and thus controls growth.

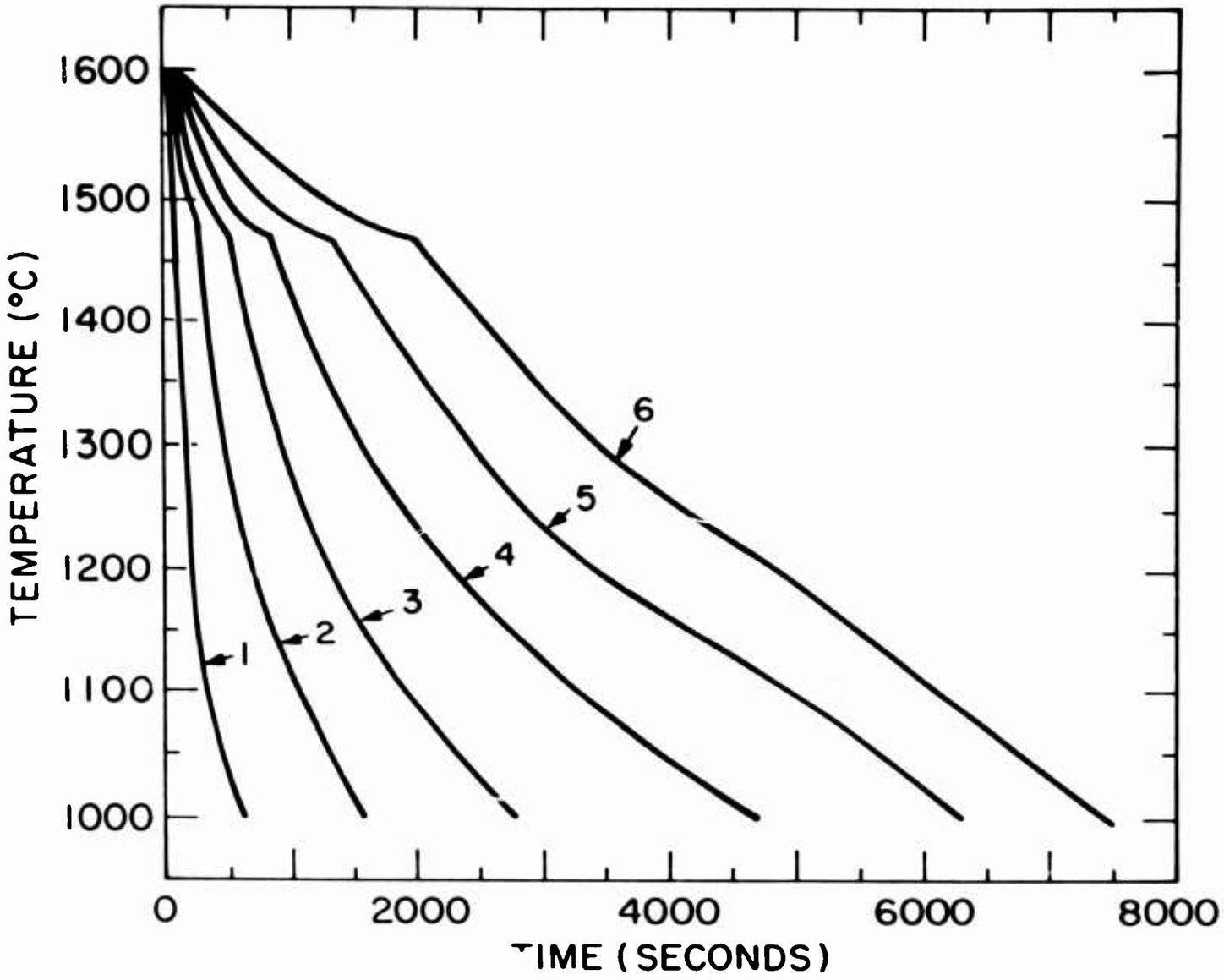

Figure 4-1: Cooling curves from the unidirectionally solidified ingot with thermocouples at 1.13, 2.17, 3.15, 4.17, 5.36, and 6.53 inches from the chill.

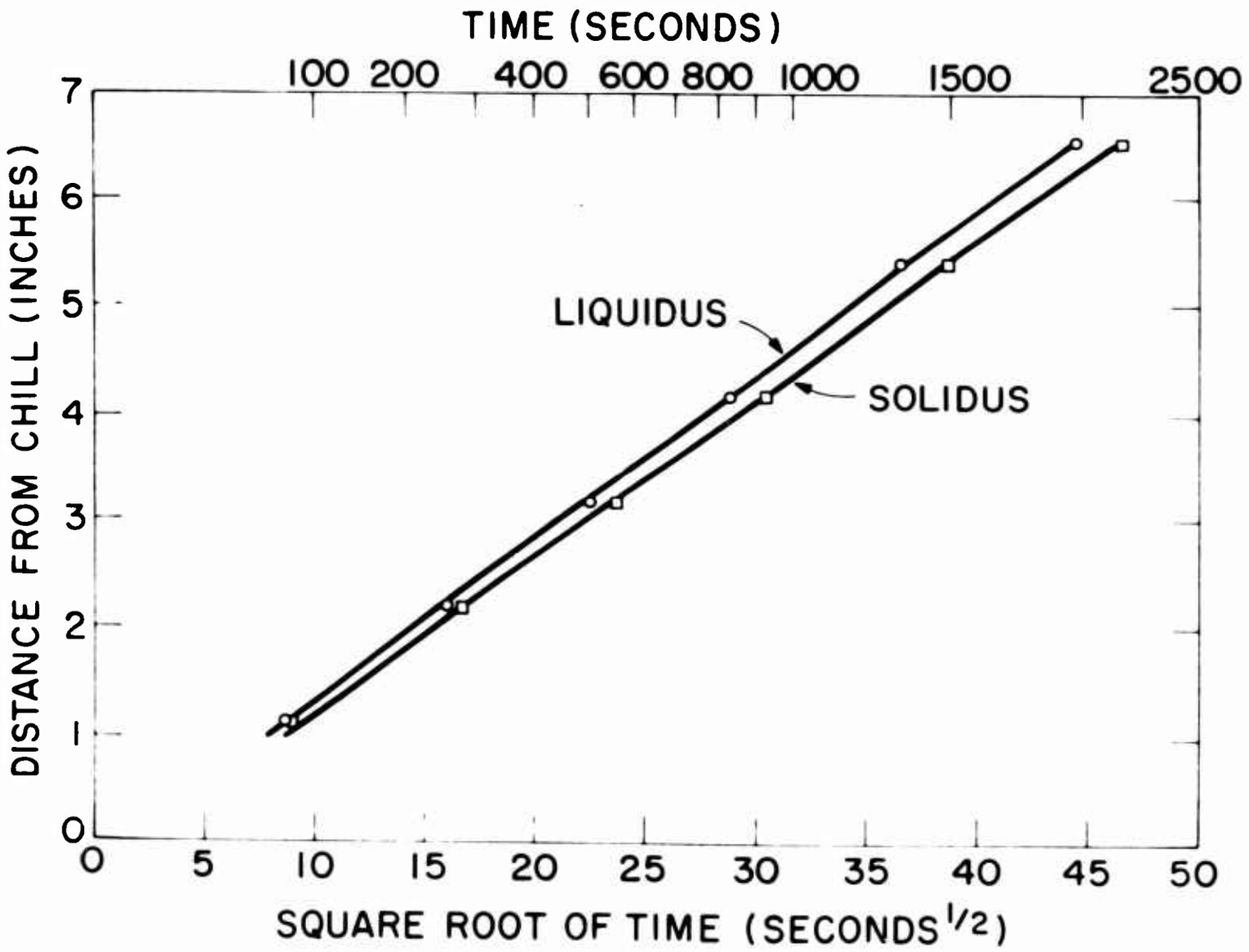

Figure 4-2: Positions of the liquidus and solidus isotherms as a function of the square root of time.

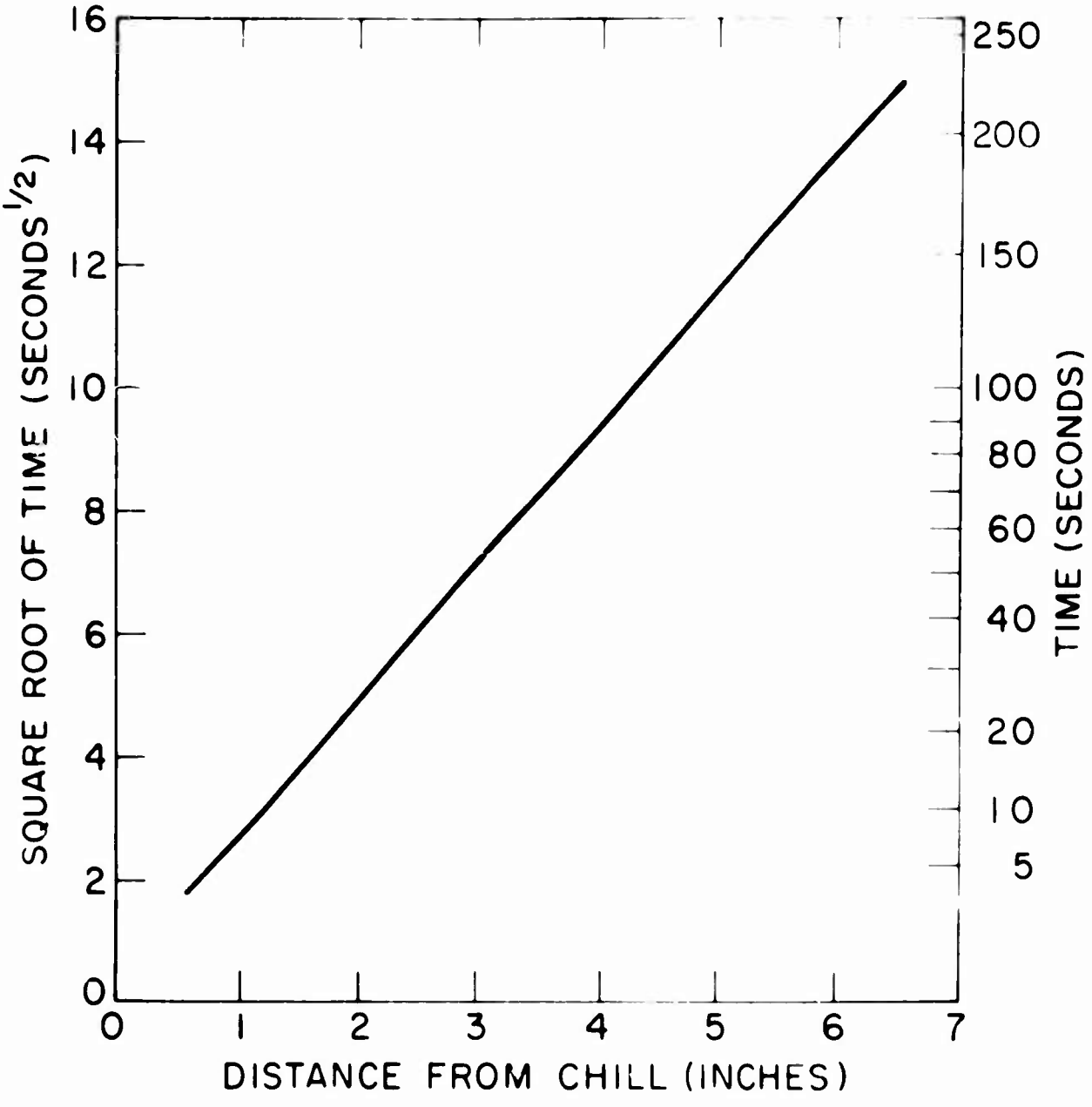

Figure 4-3: Square root of solidification time versus distance from the chill.

V. MORPHOLOGY

A. Introduction

The dendritic structure observed within cast grains (upon etching after solidification) results from microsegregation. Generally, the etch delineates lines of approximately equal concentration. In the absence of solid diffusion these isoconcentration lines (and hence the etched structure) are an accurate representation of the liquid-solid interface at various stages of solidification. Solid diffusion modifies the apparent dendrite morphology somewhat but the final apparent morphology remains an indication of the growth morphology[12].

Classically, dendrites have been represented as "rods". In this work rods that form the primary axes of dendrite elements are termed primary growth forms (primary rods, primary dendrite arms). Rods which grow perpendicular to the primary rods are secondary growth forms (secondary rods, secondary dendrite arms). Tertiary and quaternary growth forms may also be present (see Figure 5-1).

In many systems at some stages of growth, dendrite morphology is at least partly plate-like or sheet-like. Interstices between primary and secondary "arms" tend to "fill in" at an early stage of solidification; the sheets which form in this (or other) way are termed primary plates or primary sheets. Sheets oriented parallel to secondary arms and perpendicular to both primary sheets are termed

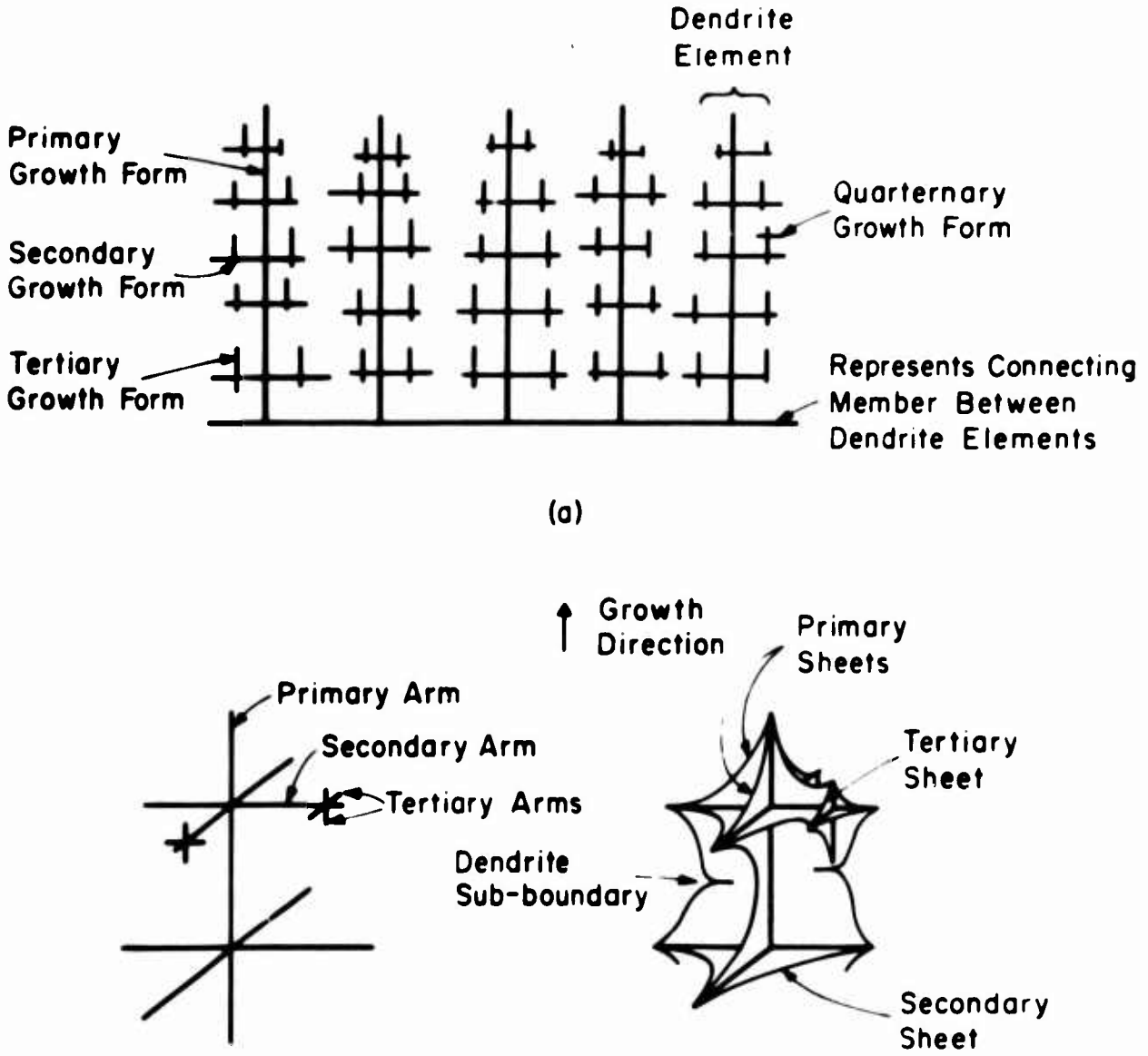

Figure 5-1: Schematic diagram of growth forms and their terminology[10].

secondary sheets; sheets containing two tertiary arms and parallel to a primary sheet are tertiary sheets.

When no secondary branches at all occur the resulting structure is sometimes termed "cellular". Several researchers have indicated that cellular structures, instead of dendritic structures, are found when the value $G_L k/C_o R_t^{1/2}$ is sufficiently low, where G_L is thermal gradient in the liquid, C_o is initial alloy content, k is the equilibrium partition ratio, and R is growth rate of the dendrite (or cell) tips[14].

B. Proce

The specimens for metallographic morphology studies were taken from the plates in one-half inch increments in planes parallel to the chill surface (transverse sections). Longitudinal sections were also taken from these same specimens across the one-inch dimension of the plate and near the center of the 5-inch dimension. The etch used for all alloys was a silute Marble's reagent.

Photomicrographs of areas 1, 2 and 4 inches from the chill surface and parallel to it and areas between 1 to 1-1/2, 2 to 2-1/2 and 4 to 4-1/2 inches from the chill surface and perpendicular to it are illustrated at both 7.6X and 34X magnification in Figures 5-2 and 5-15.

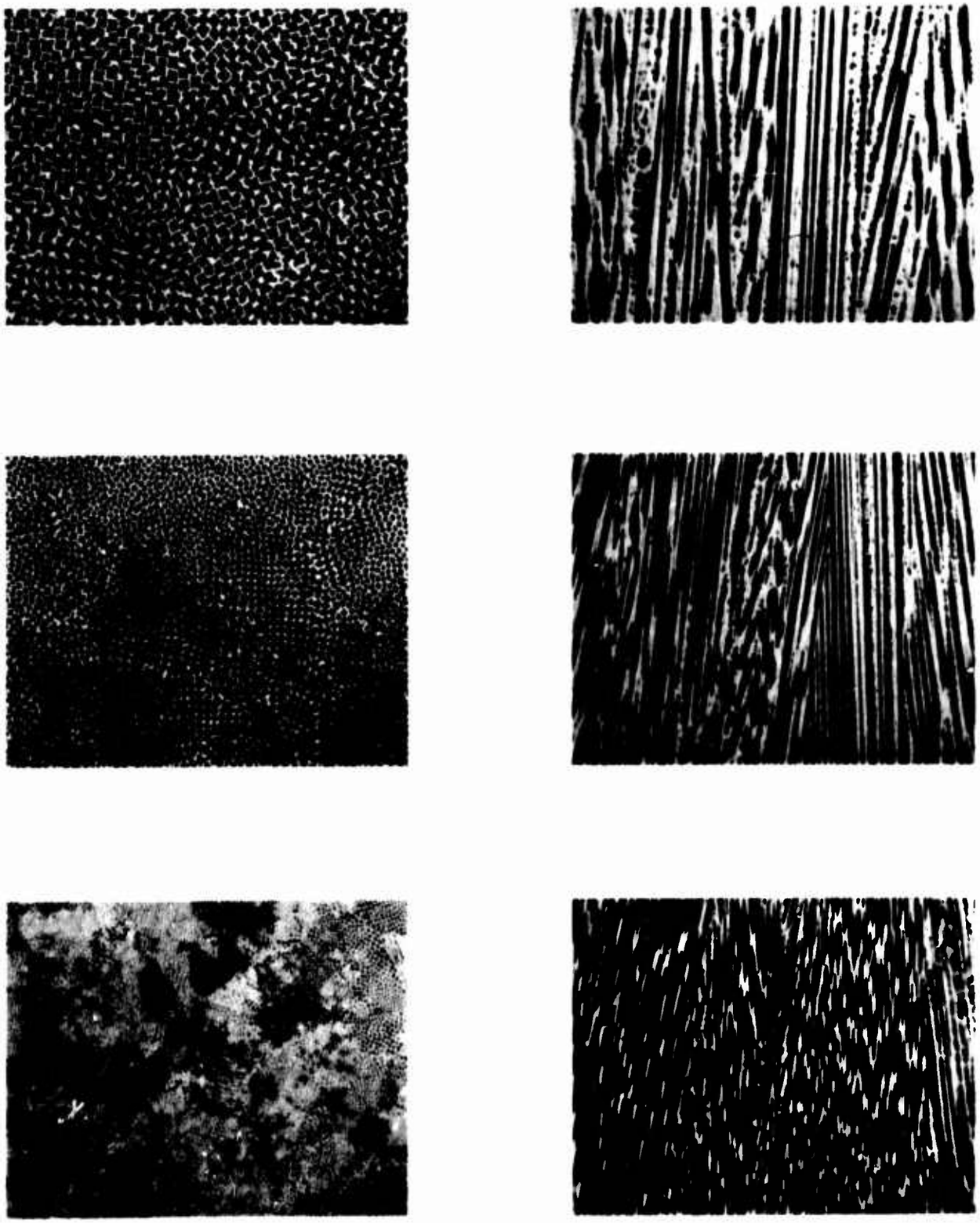

Figure 5-2: Iron-10% nickel alloy. Photographs at 1", 2" and 4" from the chill. Casting 1, 7.6X.

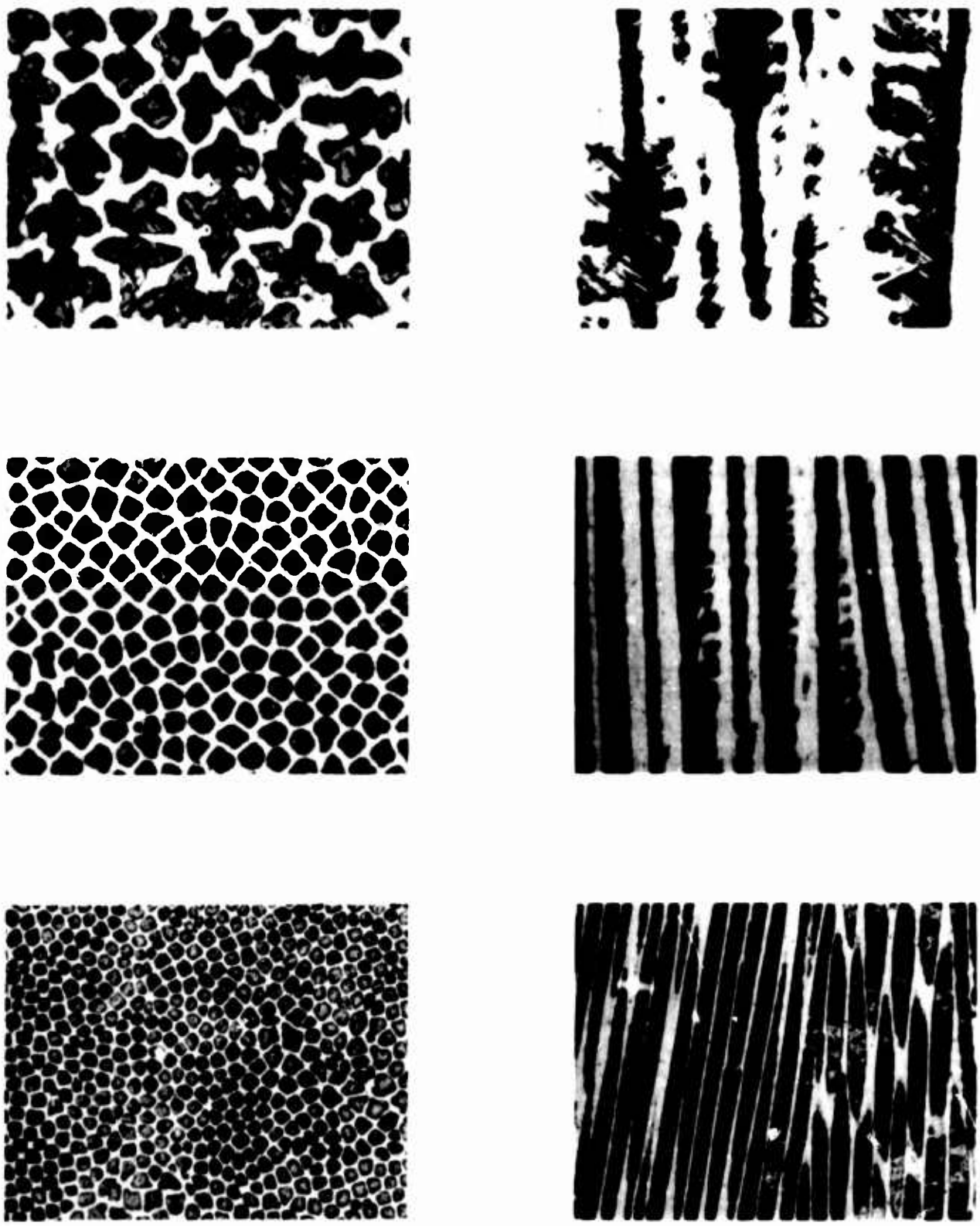

Figure 5-3: Iron-10% nickel alloy. Photomicrographs at 1", 2" and 4" from the chill. Casting 1, 34X.

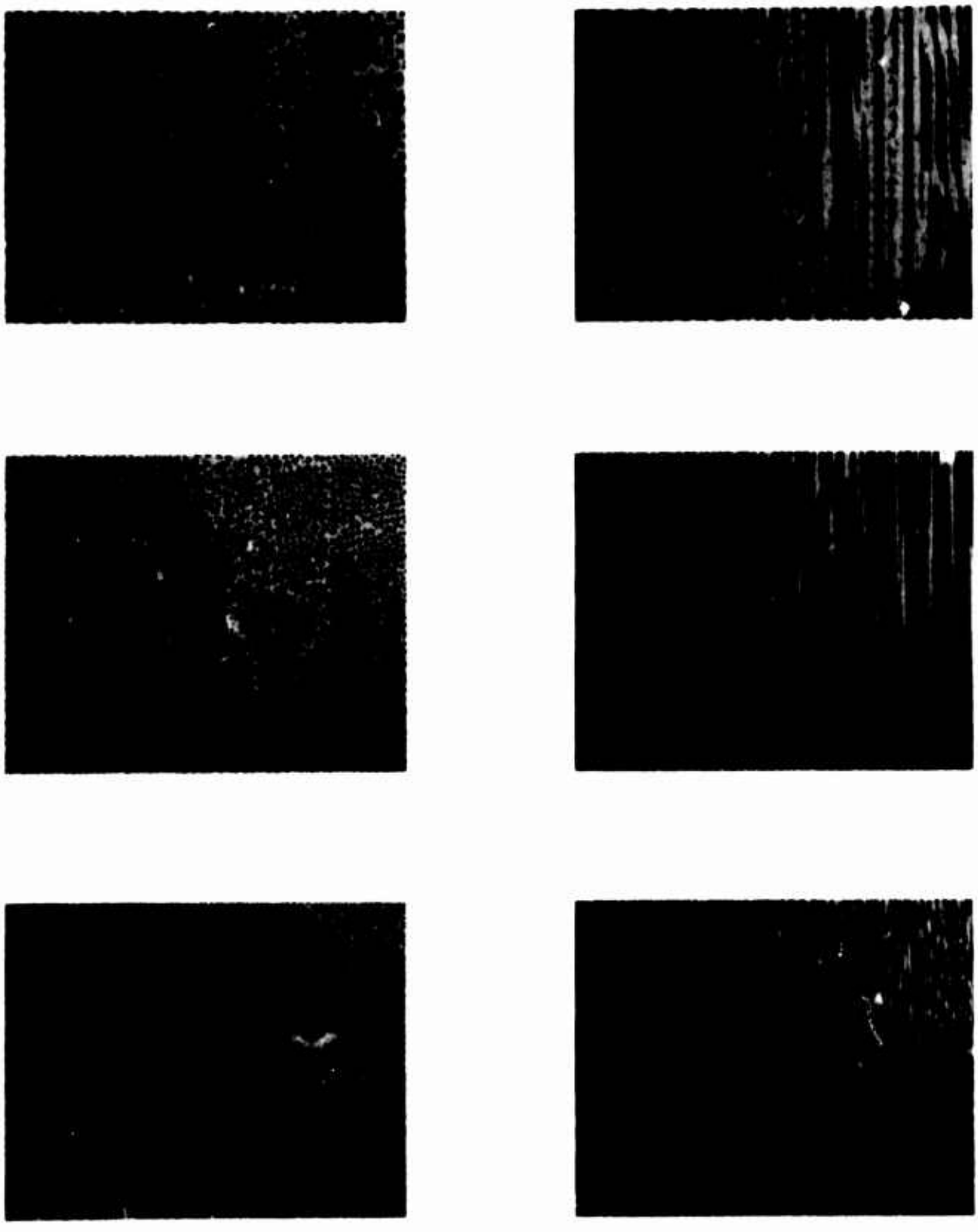

Figure 5-4: Iron-15% nickel alloy. Photomicrographs at 1" 2" and 4" from the chill. Casting 2, 7.6X.

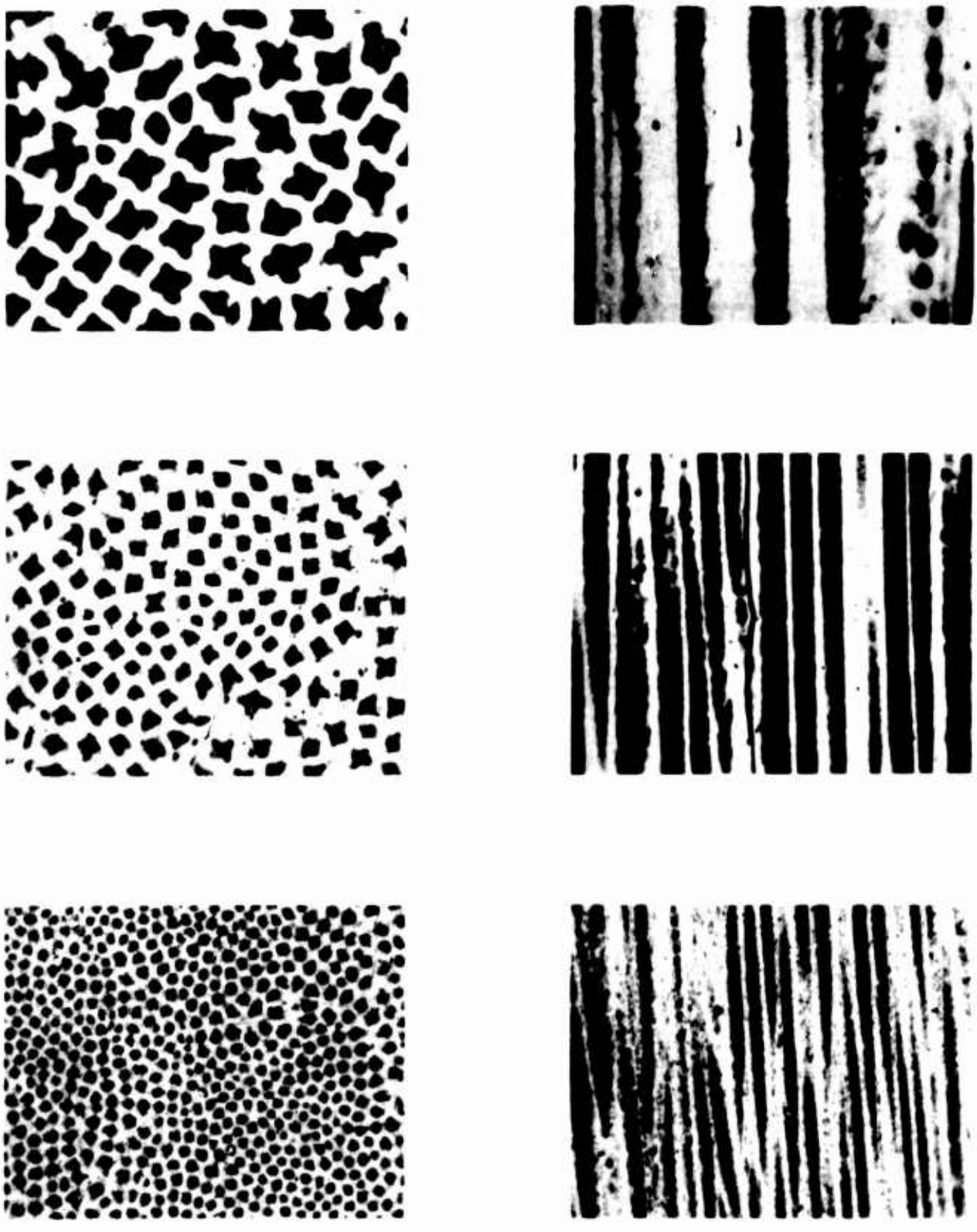

Figure 5-5: Iron-15% nickel alloy. Photomicrographs at 1", 2" and 4" from the chill. Casting 2, 34X.

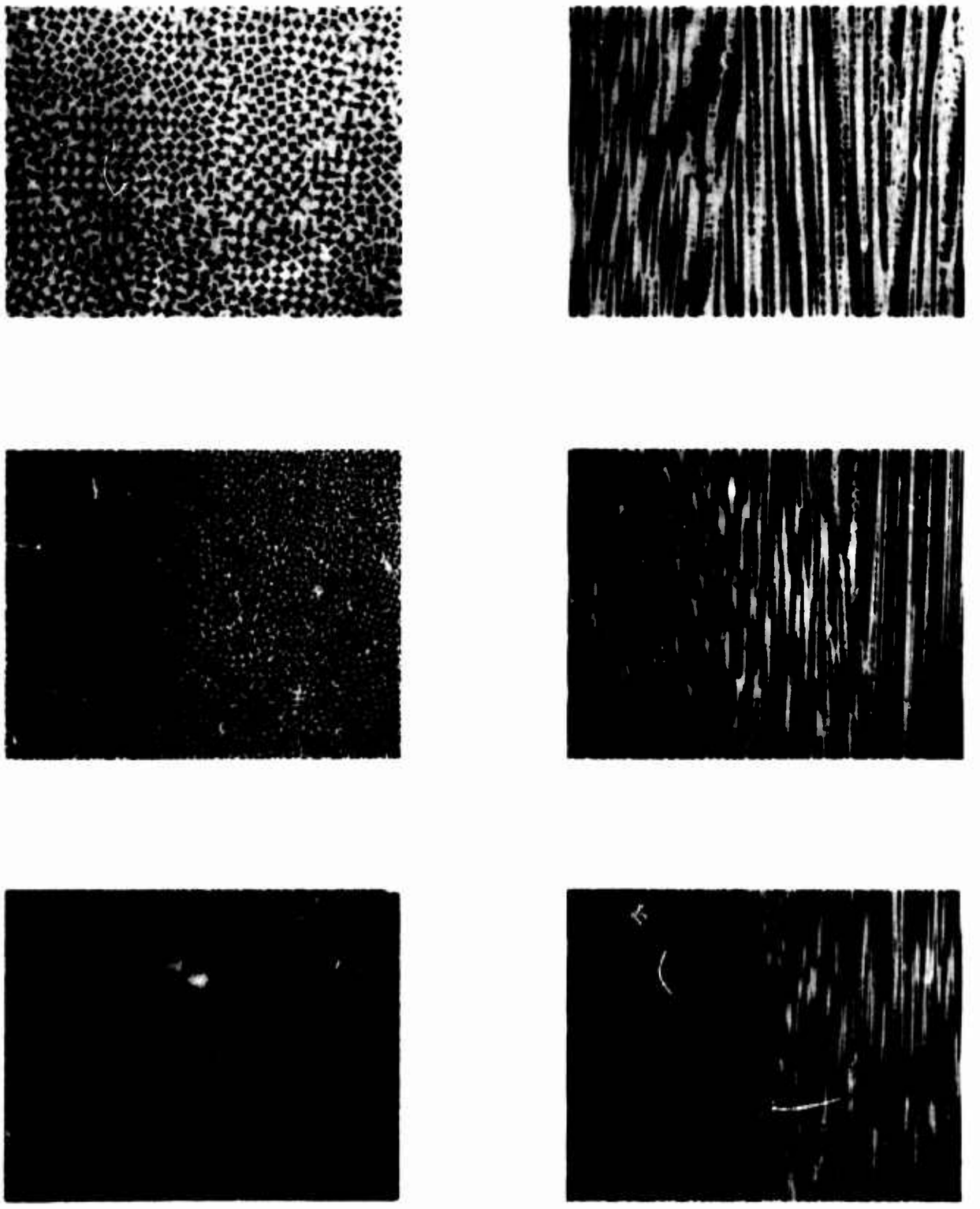

Figure 5-6: Iron-20% nickel alloy. Photomicrographs at 1", 2" and 4" from the chill. Casting 3, 7.6X.

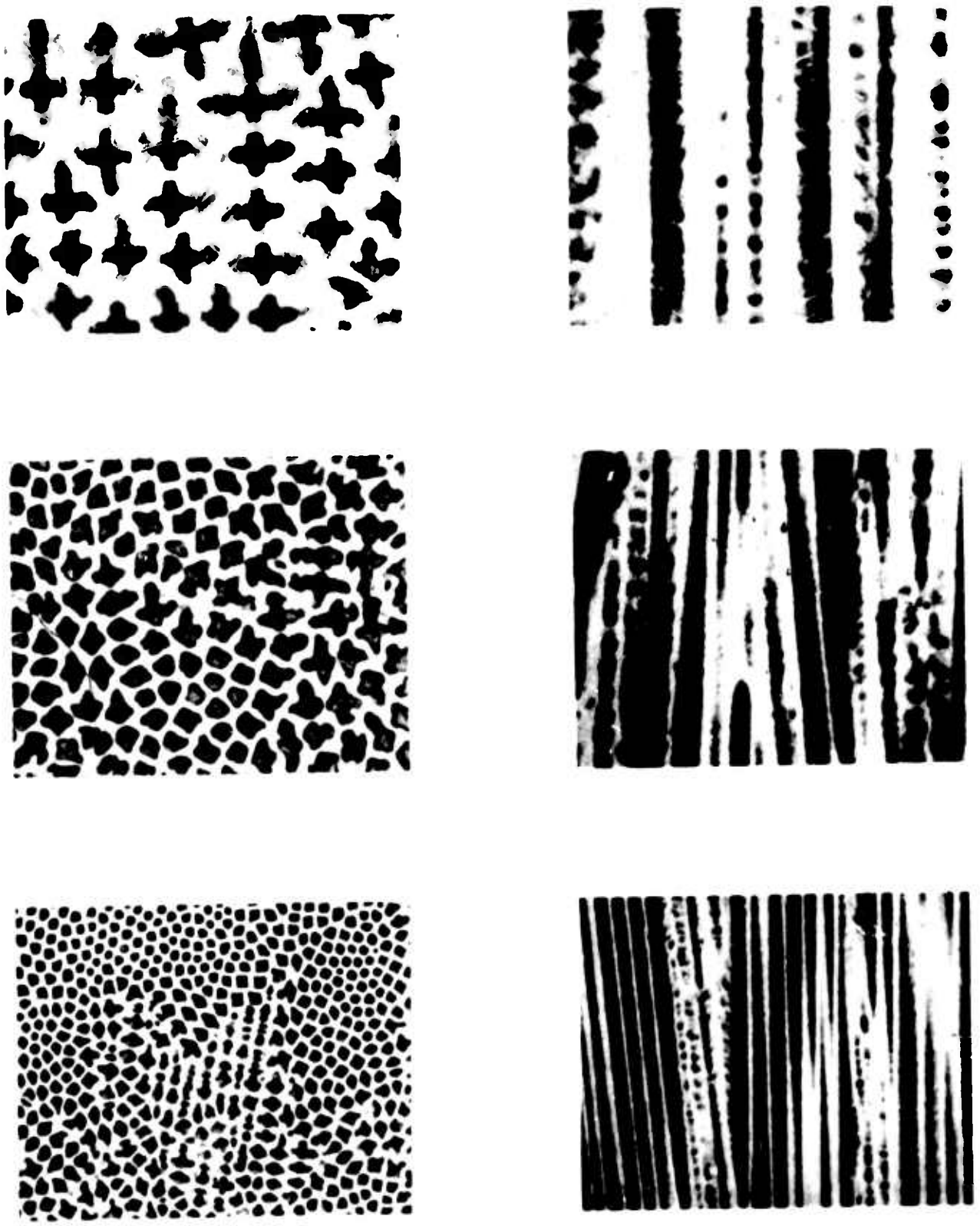

Figure 5-7: Iron-20% nickel alloy. Photomicrographs at 1", 2" and 4" from the chill. Casting 3, 34X.

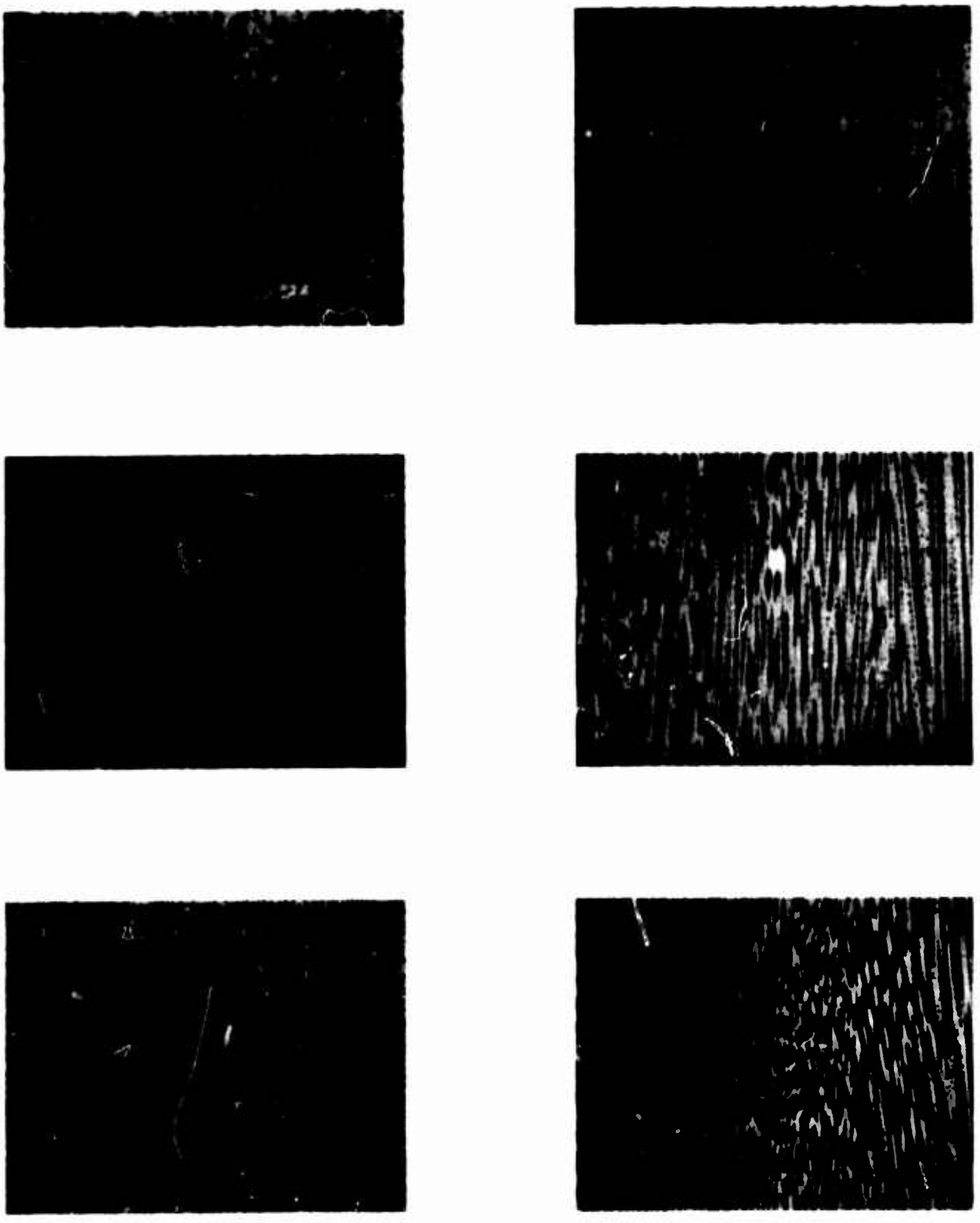

Figure 5-8: Iron-26% nickel alloy. Photomicrographs at 1" 2" and 4" from the chill. Casting 4, 7.6X.

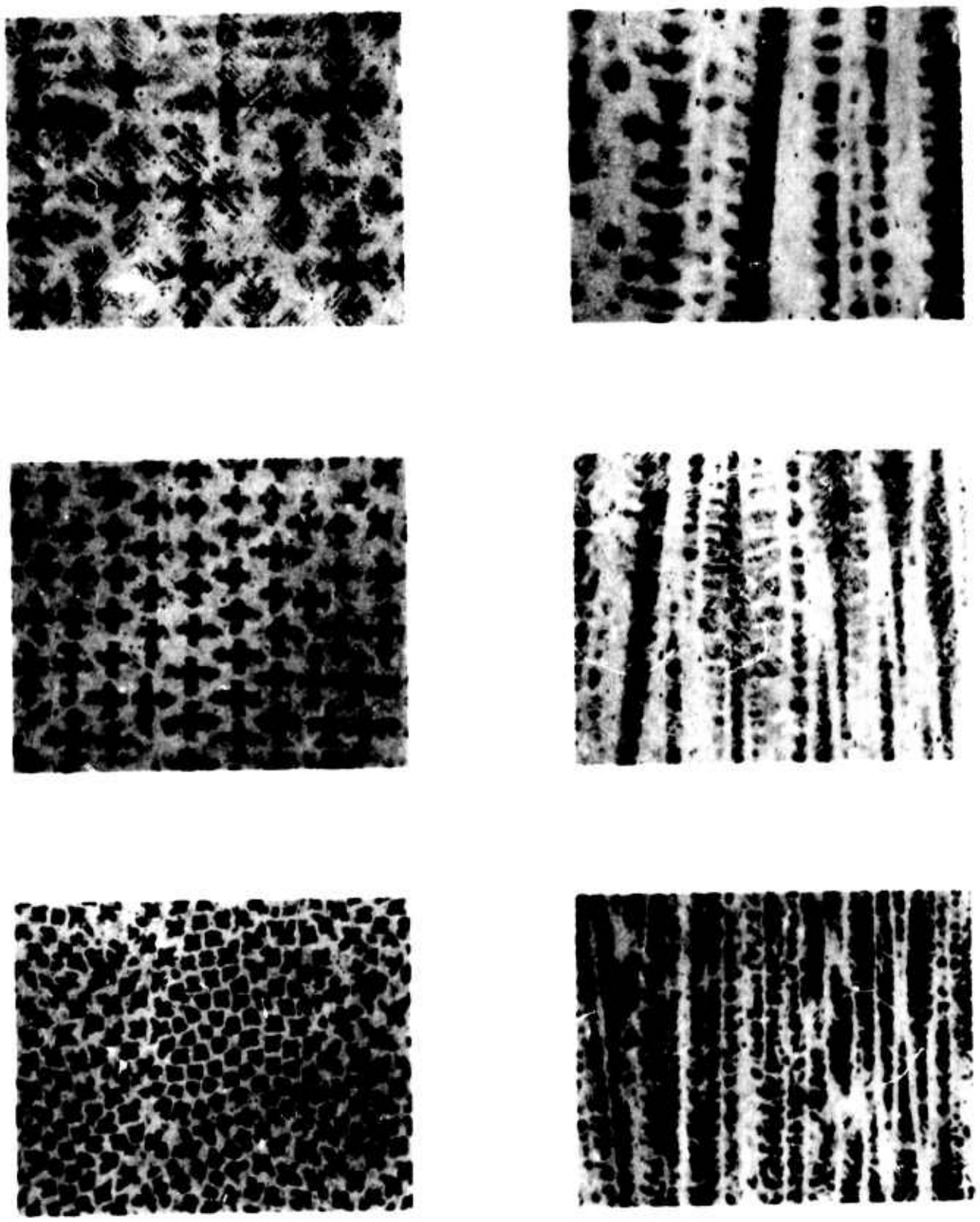

Figure 5-9: Iron-25% nickel alloy. Photomicrographs at 1", 2" and 4" from the chill. Casting 4, 34X.

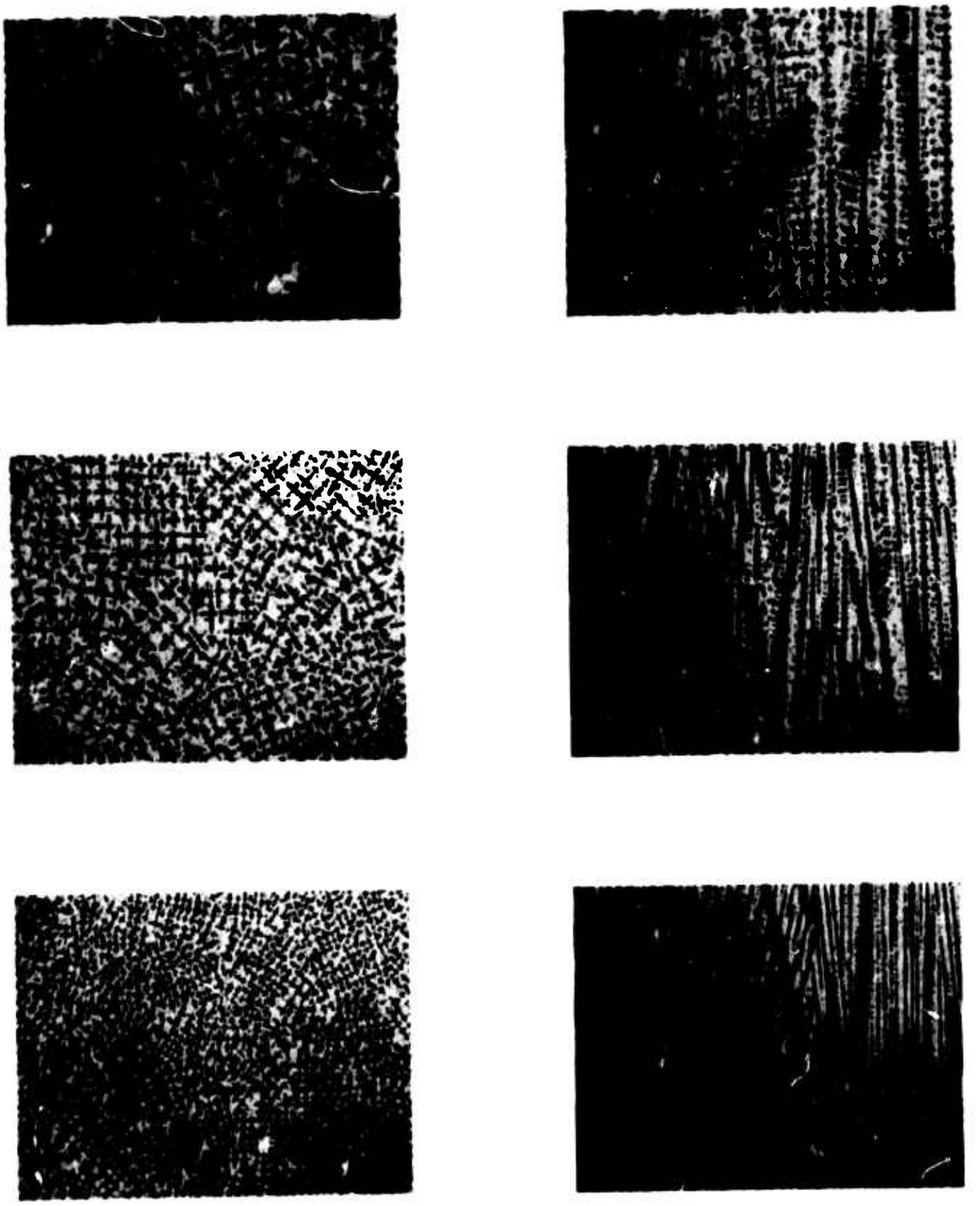

Figure 5-10: Iron-26% nickel-0.12% carbon alloy. Photomicrographs at 1", 2" and 4" from the chill. Casting 5, 7.6X.

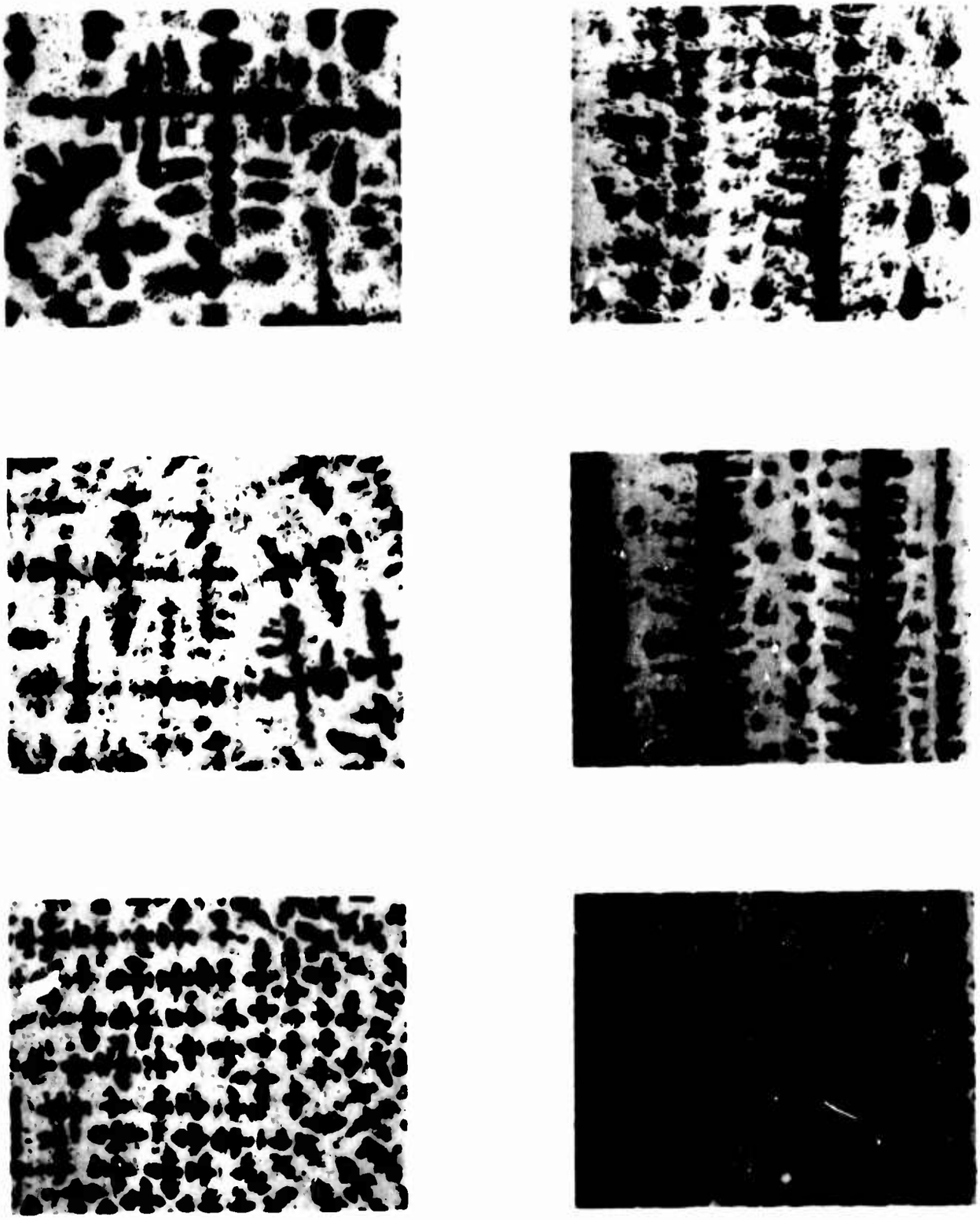

Figure 5-11: Iron-26% nickel-0.12% carbon alloy. Photomicrographs at 1", 2" and 4" from the chill. Casting 5, 34X.

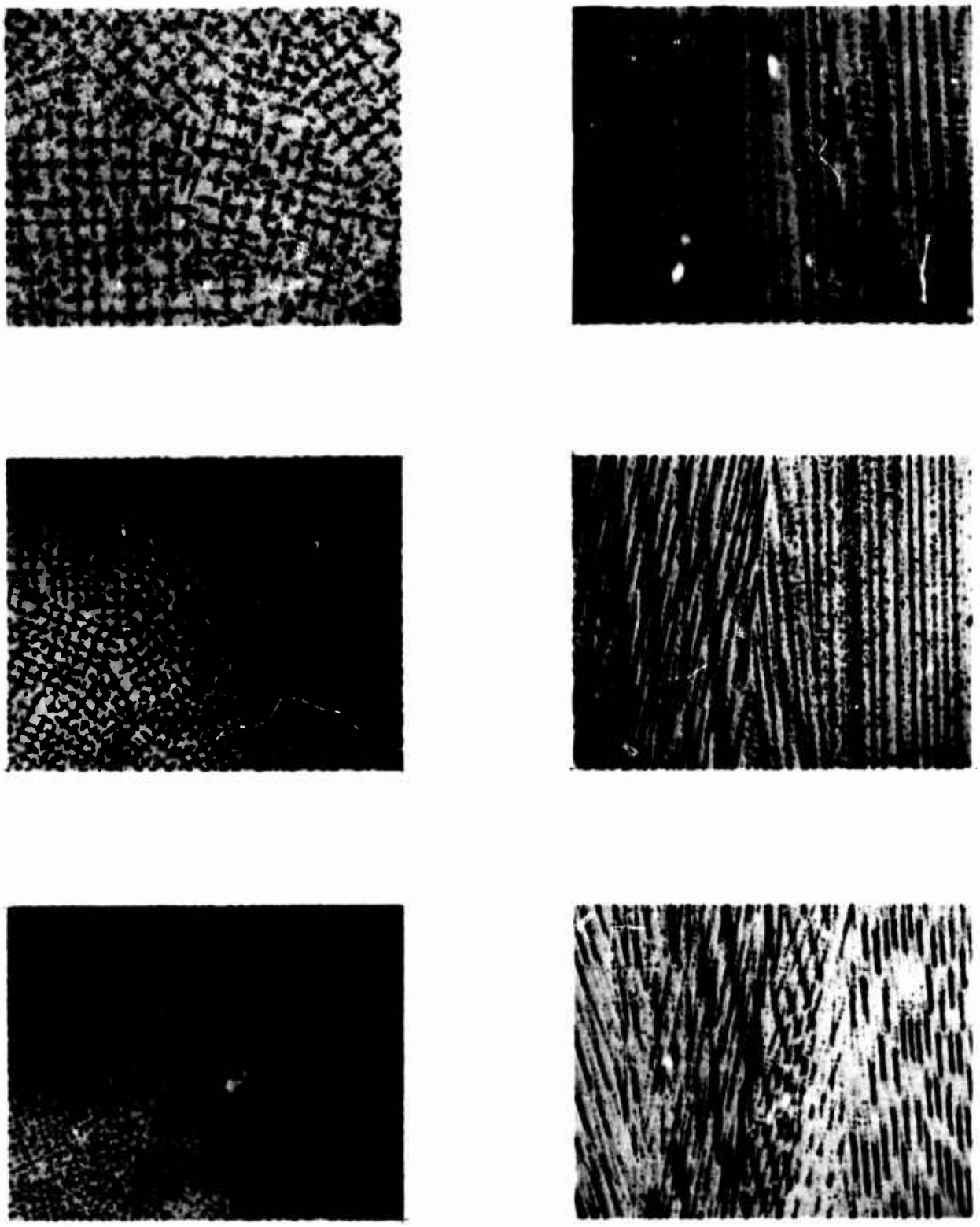

Figure 5-12: Iron-26% nickel-0.33% carbon alloy. Photomicrographs at 1", 2" and 4" from the chill. Casting 6, 7.6X.

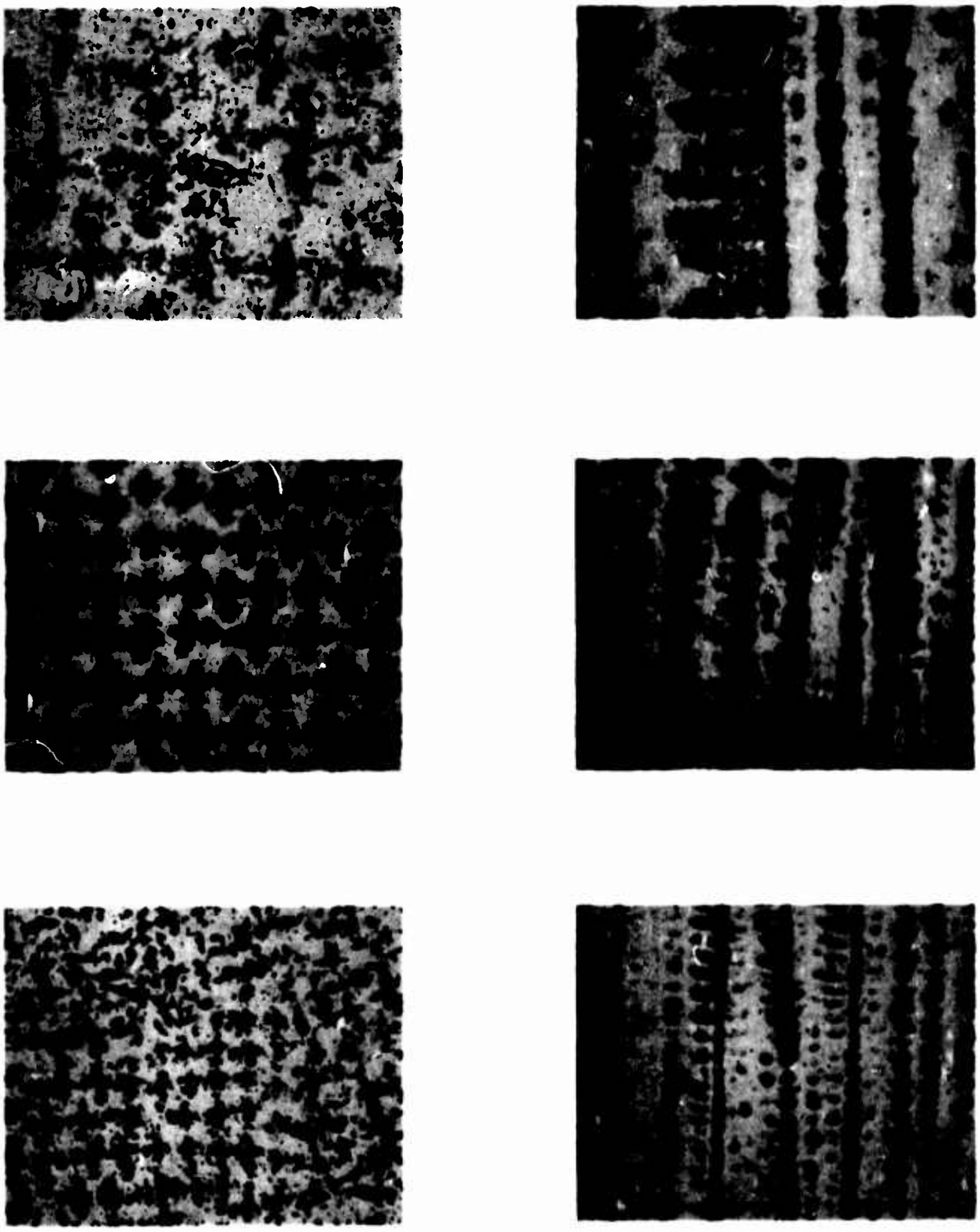

Figure 5-13: Iron-26% nickel-0.33% carbon alloy. Photomicrographs at 1", 2" and 4" from the chill. Casting 6, 34X.

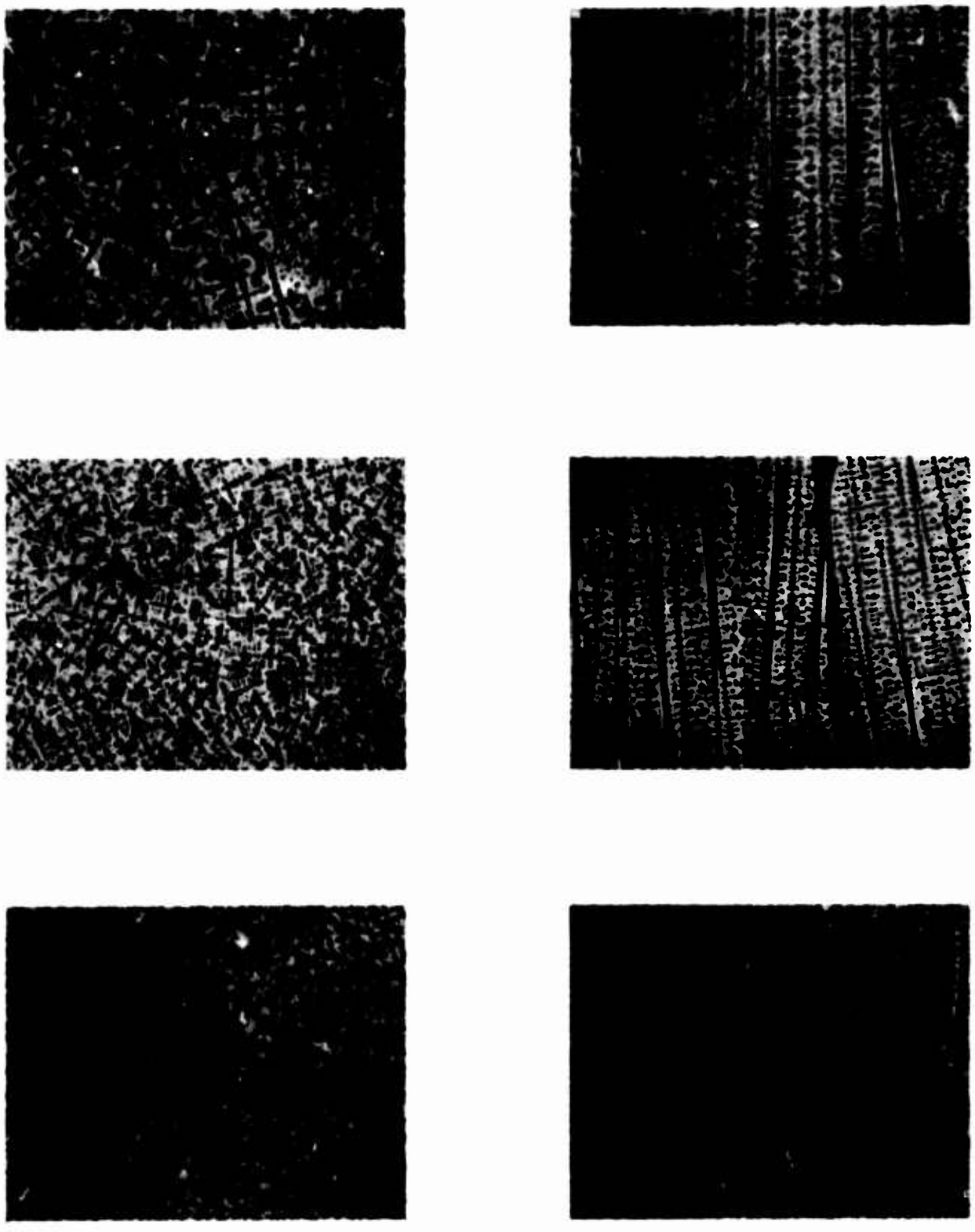

Figure 5-14: Iron-26% nickel-0.42% carbon alloy. Photomicrographs at 1", 2" and 4" from the chill. Casting 7, 7.6X.

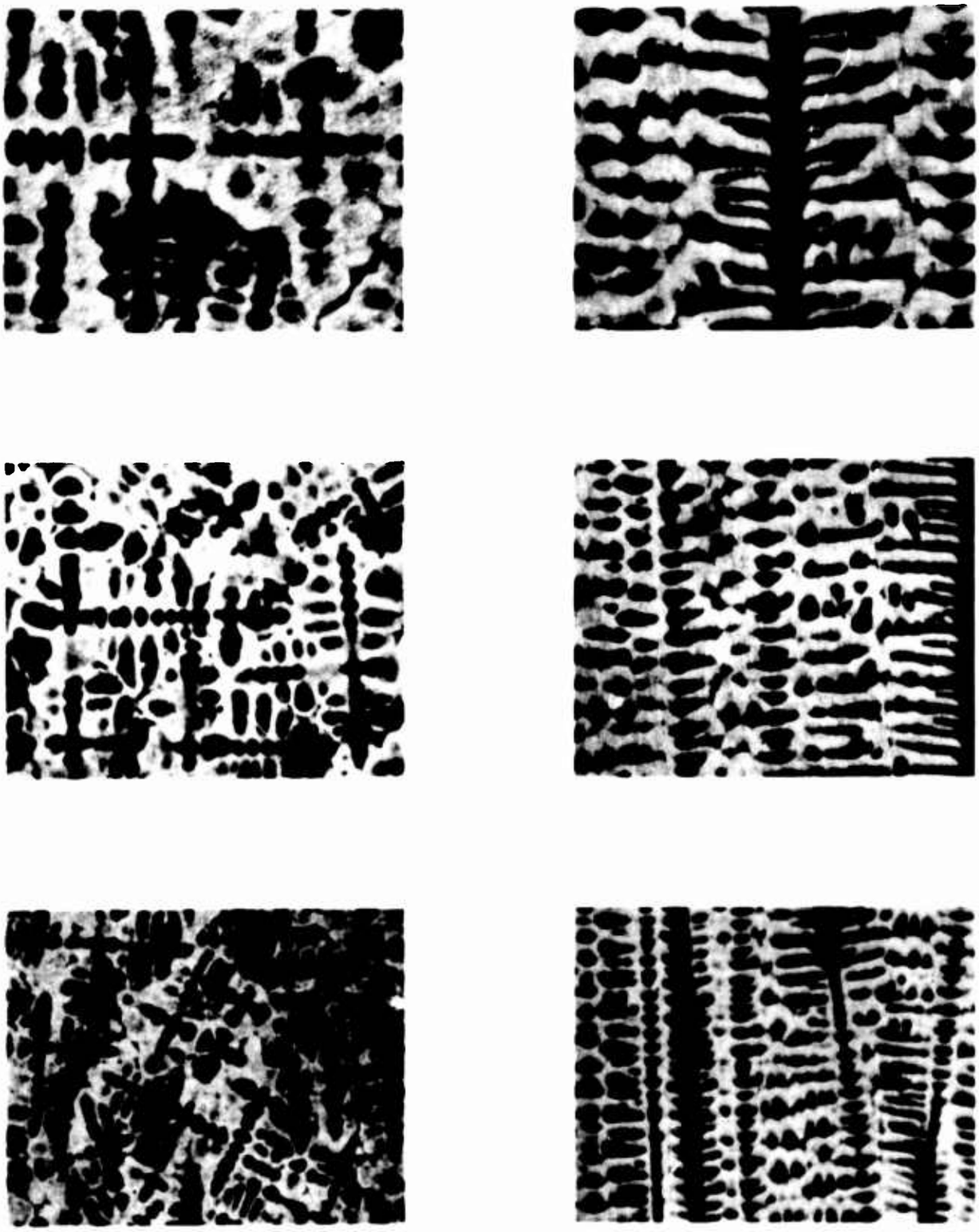

Figure 5-15: Iron-26% nickel-0.42% carbon alloy. Photomicrographs at 1", 2" and 4" from the chill. Casting 7, 34X.

C. Observations

In unidirectionally solidified castings, freezing time (time for a given location in the casting to go from liquidus to solidus temperature; note Figure 4-3) is approximately proportional to the square of the distance from the chill. Hence examination of such castings at different distances from the chill permits qualitative and quantitative correlation of structure with cooling rate.

A general observation from this work is that the dendrite structure tends to be more fully developed with increasing solidification time. In the iron-10 per cent nickel alloy (Figures 5-2, 5-3), for example, the structure appears fully cellular near the chill, with no evidence of side branching or preferential lateral growth in crystallographic directions. At distances removed from the chill, crystallographic effects begin to become evident with formation of the typical "cruciform" cross section; side branching also becomes evident.

The tendency to cell formation or minimal side growth at high cooling rates was noted in all of the alloys studied although the structure at any given cooling rate also depended on alloy content as discussed below.

The photomicrographs of ingots 1, 2, 3, and 4 (Figures 5-2 to 5-9) which contain, 10, 15, 20 and 26 per cent nickel respectively, illustrate the effect of nickel content on solidification morphology. At a given

cooling rate, increasing alloy content results in more completely formed dendritic structures. For example, the iron-10 per cent nickel alloy near the chill shows no apparent tendency toward preferential growth in crystallographic structure. As nickel content increases, the horizontal section near the chill shows a gradually more angular structure until at the 26 per cent nickel alloy, well developed cruciforms are seen, with side branching evident in the vertical section.

The ingots containing carbon (ingots 5 to 7) all exhibited larger grain sizes, dendrite spacings, and higher order growth forms than the ingot of equivalent alloy content (26 per cent nickel) that was free of carbon. Transverse sections nearest the chill contain practically no rounded cell type dendrite elemenets in the center of grains-even in the 0.12 per cent carbon alloy. Carbon also promotes tertiary growth. Within each casting the trend toward increasing dendrite complexity with increasing distance from the chill is evident.

Two methods were used to obtain primary dendrite arm spacing measurements from transverse 12X magnification photomicrographs of samples taken at one-half inch increments from the chill.

The linear method involved finding representative areas and measuring the average distance between cross centers of adjacent dendrite elements whose arms were aligned in a straight line. Cellular areas were measured by averaging the distance between cell centers. For regions consisting of complex, higher order growth forms, and larger

spacings, where primary dendrite crosses were not easily distinguished and usually unaligned, the area method was used.

The area method consisted of counting the number of primary arms contained in a given are (2 centimeters square) and calculating the spacing by assuming a simple cubic array.

Secondary dendrite arm spacing measurements were made on 12X magnification photomicrographs of longitudinal sections which exhibited regions passing through a primary dendrite core at a slight angle or those which showed the secondary arm attachment to the primary stalk. The spacing taken was that adjacent to the primary stalk.

Results of the dendrite arm spacing measurements are plotted in Figures 5-16 to 5-18 and given in Appendix B. The primary dendrite arm spacing for the 10, 15 and 20 per cent nickel alloys were very nearly the same at corresponding distances from the chill. The 26 per cent nickel alloy exhibited an increase of approximately 1.5 times the spacing of the first group. The addition of carbon generally increased the primary spacings.

Not all castings made possessed measurable secondary arms. In those that did, alloy content had little effect on spacing at locations in the first several inches from the chill. Addition of carbon tended to increase the secondary arm spacing, particularly at distances

removed from the chill, Figure 5-18. The secondary spacing was not affected by cooling rate as much as was the primary arm spacing.

D. Summary

The foregoing morphological study shows that the structure found in the iron-nickel and iron-nickel-carbon alloys is considerably more complex than the simple flat plate growth assumed in Section II for microsegregation analyses. The structure of the binary iron-nickel alloys tends to be cellular at low nickel contents and at rapid solidification rates (near the chill). At higher alloy contents and greater distances from the chill crystallographic effects become apparent with formation of the typical "cruciform" cross section, and dendritic side branching. Dendrite arm spacing generally decreased with increasing alloy content.

Addition of carbon (.12% to .42%) strongly influenced the dendritic structure. The carbon increased the primary and dendrite arm spacings appreciably and resulted in dendrites with higher order growth forms at a given cooling rate than in the carbon free alloy.

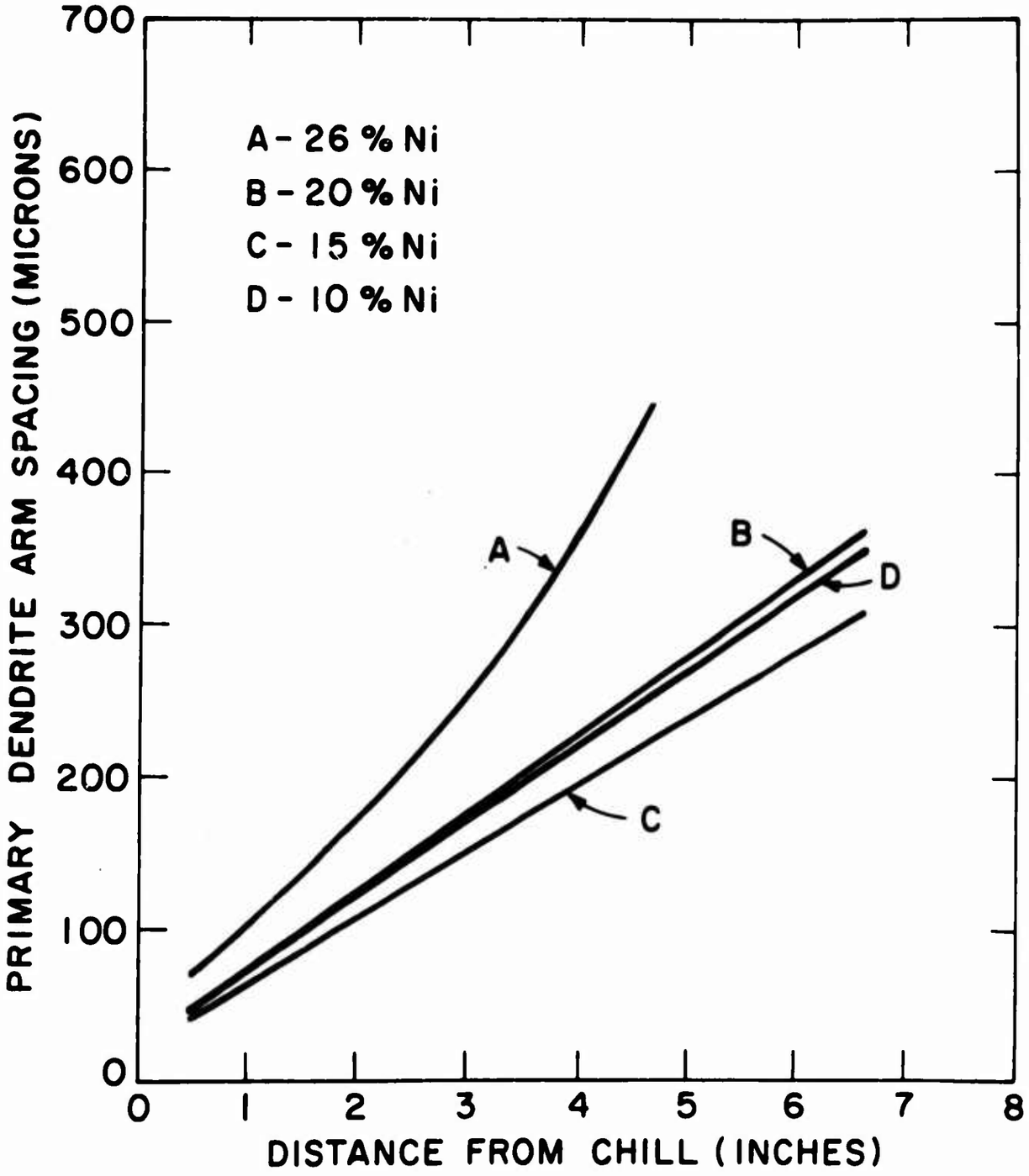

Figure 5-16: Primary dendrite arm spacing versus distance from the chill for binary iron-nickel alloys.

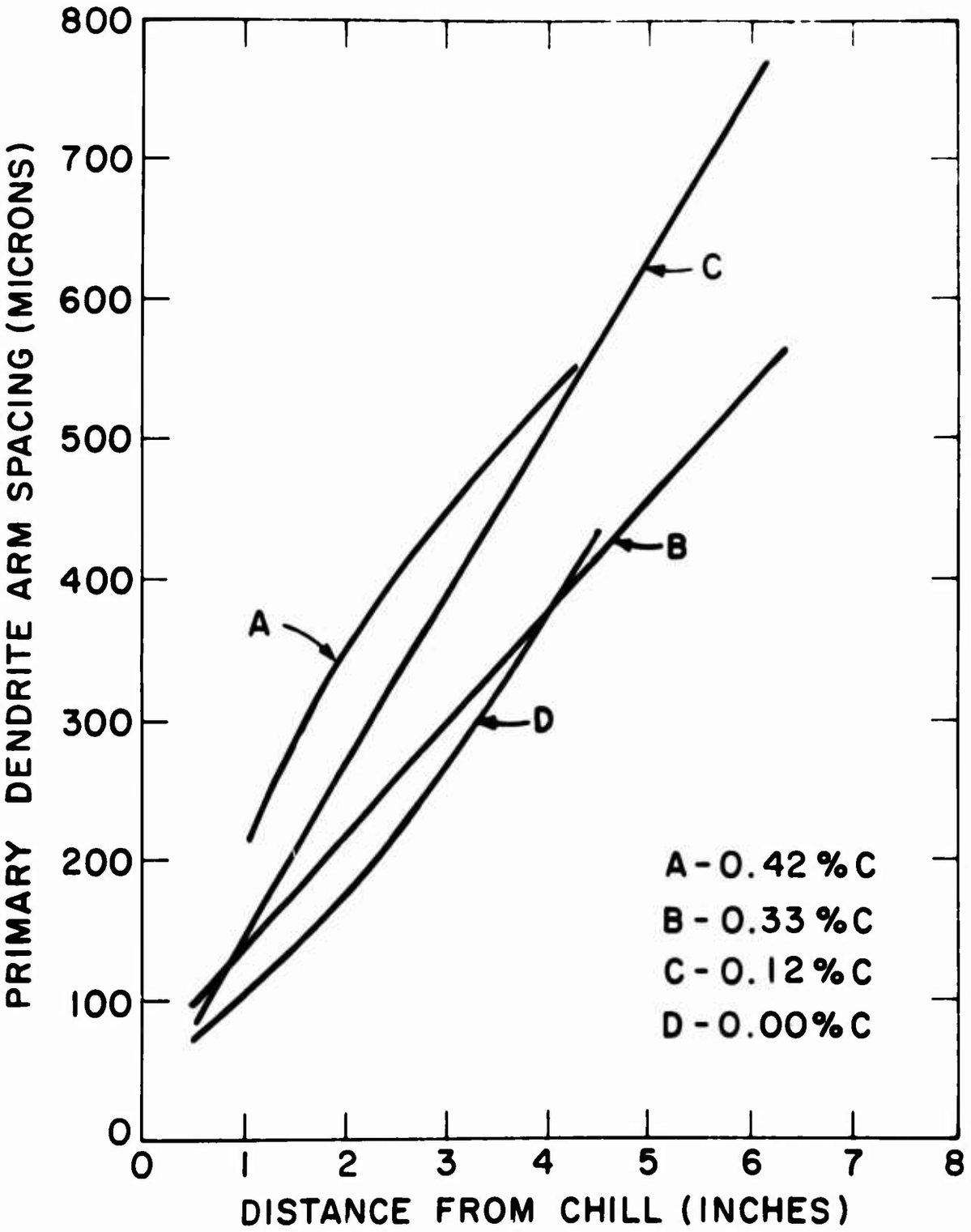

Figure 5-17: Primary dendrite arm spacing versus distance from the chill for ternary iron-nickel-carbon alloys containing 24-26 per cent nickel.

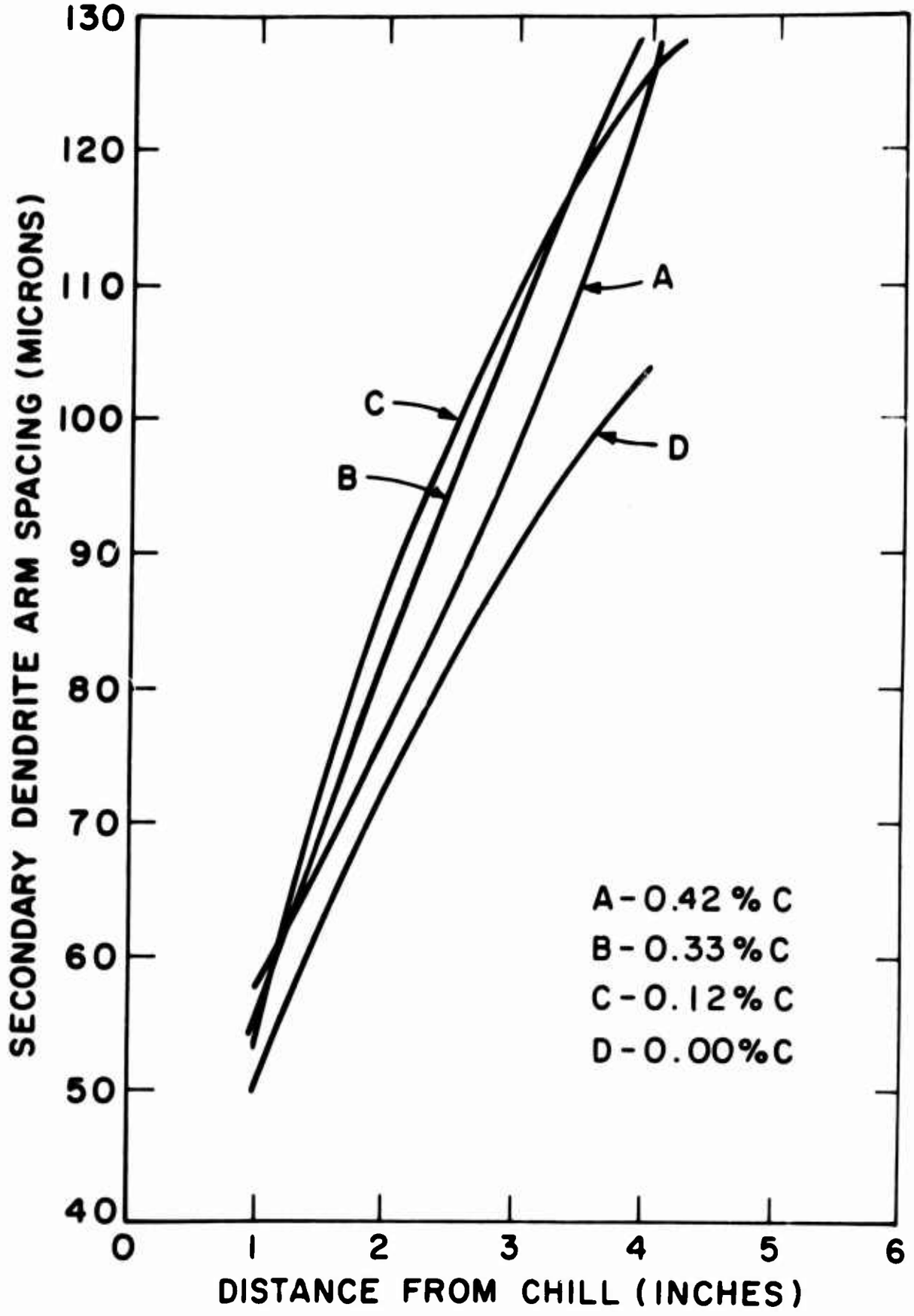

Figure 5-18: Secondary dendrite arm spacing versus distance from the chill for iron-nickel-carbon alloys, containing 24-26 per cent nickel.

VI. MEASUREMENTS OF MICROSEGREGATION IN IRON-NICKEL ALLOYS

A. Procedure

The chemical segregation existing in the binary iron-26 per cent nickel casting was determined experimentally by electron microprobe analysis. Microprobe traces were made on four samples taken in a plane perpendicular to the primary growth direction (parallel to the chill surface). The maximum and minimum nickel values were measured and "Segregation Ratio" calculated

1. Scanning Techniques.

A commercial electron microprobe* with a one micron focal spot and a 52.5° take-off angle was used for microscopic chemical analysis.

To obtain values of C_M° and C_m° metallographic samples were etched and microhardness marks made as references. The samples were lightly polished to remove the etched surface and then probed. Probe paths were chosen parallel to the cross arms forming the central portion of the dendrite. Since the maximum solute content may deviate from the center of the interdendritic region, the initial path was hand scanned until a maximum was reached; then at this point a path perpendicular to the original was run to find a maximum in this path. Orthogonal paths were continually made at each maximum until the

---

* Applied Research Laboratory Electron Microprobe Analyzer.

actual maximum was determined. A similar scanning process was used for obtaining C'_m. This procedure is identical to that used by Kattamis[1,2].

Iron and nickel contents were determined simultaneously, providing a means of distinguishing true minimum nickel values from low nickel readings caused by pores or inclusions. A set of standards of known chemical compositions including samples of pure iron and pure nickel were run prior to probing each specimen. A check for probe stability was made by at least running the pure nickel and pure iron after each specimen and allowing no more than a 5 per cent drift in intensity. When two or more specimens were run the standards were run alternately to provide good working curves in addition to checking for probe stability.

A fixed 30 second accumulation time, which ammassed a total of between 20,000 and 40,000 counts for the unknown, was used in combination with scanning steps varying from 2 to 8 microns depending on the concentration gradient. The minimums in all cases had more shallow gradients than the maximums, permitting the use of larger scanning steps. Maximum and minimum values were determined in several positions within the sample

B. Microprobe Results and Comparison with Theory

Results of the electron microprobe analysis are listed in Table 6-1. Minima (at the center of dendrite arms) were essentially

constant at locations from 1/2 inch to 4 inches from the chill. Maxima (at interdendritic regions) decreased with increasing distance from the chill and so segregation ratio, S_o, decreased also.

The statistical error based on the number of counts taken was calculated for each measurement assuming it to be $2\sqrt{\frac{1}{N_U} + \frac{1}{N_S}}$, where N_U = total number of counts taken at given point on specimen and N_S = total counts taken on known standard. These values are listed in Table 6-1.

The minimum nickel values in Table 6-1 are significantly higher than those estimated by the equilibrium phase diagram for an alloy of 26 per cent nickel (C_m° = 19.3 per cent nickel). This deviation must be due to solid state diffusion which occurs both during solidification and while cooling to room temperature.

Table 6-2 compares results of experimental measurements in Table 6-1 with theory as obtained earlier. Specifically, comparison is made of measured segregation ratio (S_e°) with calculated segregation ratio (S_c°) as determined from Figure 2-10. As discussed previously[6] the assumption of a simple platelike dendrite geometry employed herein prevents quantitative agreement of experiment with theory unless the measured dendrite arm spacing is multiplied by a "geometric correction factor"; g, to compensate for multidimensional diffusion. A suitable geometric correction factor for aluminum-copper alloys over a wide range of solidification condition was shown to be 0.32.

TABLE 6-1

Electron Microprobe Analyzer Results

Specimen	Distance from Chill - Inches	C°_{M} (%Ni)	C°_{m} (%Ni)	S°_{e} $C^{\circ}_{M}/C^{\circ}_{m}$
4 - 1	1/2	32.6 ± .57	25.5 ± .47	1.28 ± .03
4 - 3	1	30.0 ± .55	24.5 ± .47	1.22 ± .03
4 - 4	2	29.5 ± .54	25.2 ± .49	1.17 ± .03
4 - 9	4	29.8 ± .53	25.2 ± .47	1.18 ± .03

Comparison of Measured and Theoretical Segregation Ratios, Iron-26% Nickel Alloy

Calculations Based on Primary Arm Spacing:

Location X (inches)	Solidification Time, θ_f (seconds)	Dendrite Arm Spacing, d ($cm \times 10^4$)	γ_e (c) ($cm^2 sec^{-1} \times 10^8$)	γ_c (d) ($cm^2 sec^{-1} \times 10^8$)	S_e^*	S_c^* (e)
1/2	2.6	73 (b)	2050	4.9	1.28	1.28
1	7.3	110 (b)	1660	4.0	1.22	1.22
2	24.1	160 (b)	1070	2.6	1.17	1.16
4	86.6	350 (b)	1440	3.4	1.18	1.20
Calculations Based on Secondary Arm Spacing:						
1/2	2.6	40 (f)	615	8.7	1.28	1.4
1	7.3	51 (f)	356	5.0	1.22	1.3
2	24.1	72 (f)	220	3.1	1.17	1.2
4	86.6	104 (f)	130	1.8	1.18	1.1

(a) Taken from Figure 4-3.

(b) Measured primary arm spacing, Figure 5-16.

(c) $\gamma_e^2 = d^2/\theta_f$.

(d) $\gamma_c^2 = (gd)^2/\theta_f = (g\gamma_e)^2$, where g is a "geometric correction factor" taken here as 0.05 for primary arms and 0.12 for secondary arms.

(e) Taken from Figure 2-10.

(f) Measured secondary arm spacing: Figure 5-18.

In Table 6-2, comparison of experiment and theory is made on the bases of both measured primary and secondary dendrite arms. Best agreement of experiment with theory is obtained when the geometric factor, g, is .05 when considering primary arm spacing and 0.13 when considering secondary spacing.

The low geometric factors apparently result from the complexity of the dendrite geometry as compared with the single parallel plate model, and perhaps to changing morphology with increasing solidification time. Present experimental and theoretical work is directed at this problem.

Data for equiaxed structures from a previous annual report[9] are analyzed in Table 6-3, in the same manner as the foregoing. These data are for much longer solidification times (185 to 6000 seconds). Approximate agreement with theory is obtained using the measured secondary dendrite arm spacings and a geometric correction factor, $g = 0.32$.

TABLE 6-3

Comparison of Measured and Calculated Segregation Ratios, Slowly Solidified Iron-26% Ni Alloy[9]

Cooling Rate (°C/sec)	Solidification Time, θ_f[(a)] (seconds)	Dendrite Arm Spacing, d[(b)] (cm x 10^4)	γ_e^2[(c)] ($cm^2 sec^{-1} \times 10^8$)	γ_c^2[(d)] ($cm^2 sec^{-1} \times 10^8$)	S'_e	S°_c
.14	5	77	32	3.2	1.23	1.20
.06	400	145	54	5.4	1.25	1.30
.004	5870	280	134	13.4	1.15	1.50

(a) Calculated assuming a non-equilibrium freezing range of 25°C.

(b) Secondary dendrite arm spacing.

(c) $\gamma_e^2 = d^2/\theta_f$.

(d) $\gamma_c^2 = (g\gamma_e)^2$, where g, the "geometric correction factor" is taken here as .32.

(e) Samples were quenched from 55°C below the liquidus.

VII. CONCLUSIONS

1. A numerical technique has been employed to compute microsegregation in alloys in which (a) the final solidification temperature and composition is variable, and (b) substantial diffusion occurs in the solid during and after solidification.

2. In iron-26 per cent nickel alloy, segregation ratio obtained is from 1.15 to 1.28 depending on solidification conditions. These results are in qualitative agreement with theory. Quantitative agreement requires use of a geometric correction factor; improved quantitative agreement is believed to depend on employment of an improved dendrite model in computer calculations.

3. Dendrite morphology was examined in iron-nickel alloys containing from 10 to 26 per cent nickel, and in iron-nickel-carbon alloys containing about 26 per cent nickel and up to 0.42 per cent carbon.

4. "Cellular" structures result in the alloys studied under conditions of low solute content and high cooling rate. Lower cooling rates and higher solute contents produce a more complex dendrite structure, with secondary and tertiary branching.

5. Primary dendrite arm spacing in the ingots studied ranged from about 40 to 700 microns, depending on alloy analysis and cooling rate. Dendrite arm spacing in the alloys studied generally increase with (a) decreasing cooling rate, (b) increasing nickel content (at least in the range of 15 to 26 per cent nickel, and (c) carbon additions.

BIBLIOGRAPHY

1. "Investigation of Solidification of High Strength Steel Castings," M.I.T., Interim Report, Contract No. DA-19-020-ORD-5443(X), Army Materials Research Agency, October, 1963.

2. T. Z. Kattamis, M. C. Flemings, "Dendrite Morphology, Microsegregation, and Homogenization of Low Alloy Steel," Trans. AIME, V. 233, 1965, pp. 992-999.

3. F. C. Quigley, P. J. Ahearn, "Homogenization of Steel Castings at 2500°F," Trans. AFS, V. 72, 1964, pp. 813-817.

4. H. D. Brody, M. C. Flemings, "Investigation of Parameters Influencing Solidification of Aluminum Base Alloys," Annual Report, M.I.T., Contract No. DA-19-020-ORD-5706(A), Frankford Arsenal, July, 1963.

5. T. F. Bower, H. D. Brody and M. C. Flemings, "Effect of Solidification Variables on the Structure of Aluminum Base Alloys," Annual Report, Contract No. DA-19-020-ORD-5706(A), Frankford Arsenal, June, 1964.

6. H. D. Brody, T. F. Bower and M. C. Flemings, "Measurement of Solute Redistribution in Dendritic Solidification," submitted for publication, Trans. Met. Soc., AIME.

7. R. W. Floyd, "The Equilibrium Diagram of the System Iron Nickel," Annotated Equilibrium Diagrams, No. 11, The Institute of Metals, 1955.

8. J. F. Elliott, M. Gleiser and V. Tamakrishna, Thermochemistry for Steelmaking, Addison Wesley Publishing Co., Inc., 1963.

9. "Investigation of Solidification of High Strength Steel Castings," M.I.T. Interim Report, Contract No. DA-19-020-ORD-5443, Army Materials Research Agency, October, 1962.

10. J. I. Goldstein, Sc.D. Thesis, M.I.T., June, 1964.

11. R. F. Polich, G. E. Nereo and M. C. Flemings, "Directional Solidification Studies," Final Report, Foundry Section, Metals Processing Division, Department of Metallurgy, M.I.T., Department of the Army, Ordnance Corps., Contract No. DA-19-020-AMC-5753(Z).

12. B. P. Bardes, Sc.D. Thesis, Department of Metallurgy, M.I.T., 1965.

13. For historical review, see T. F. Bower, Sc.D. Thesis, Department of Metallurgy, M.I.T., 1965.

14. T. S. Plaskett and W. C. Winegard, Can. J. Phys., V. 37, 1555, 1959.

APPENDIX A

List of Symbols

α	$\frac{D_s \theta_f}{\ell^2}$
b	$\frac{G_L D_L}{R_t m_L}$
C_m', C_m°	minimum solute concentration in solid dendrite at the non-equilibrium solidus and room temperature, respectively
C_M', C_m'	maximum solute concentration in solid dendrite at the non-equilibrium solidus and at room temperature, respectively
C_L^*, C_s^*	concentration of solute at the interface in the liquid and solid, respectively
C_o	initial alloy content
C_P	heat capacity of solid
C_s	composition at some point within the solid phase
$\bar{C}_s$	average composition of the solid phase
d	dendrite arm spacing
D_S, D_L	diffusion coefficient of solute in solid and liquid phases, respectively
f_s	weight fraction of solid phase
g	geometric correction factor
γ^2	$(2\ell)^2/\theta_f$
G_L	temperature gradient in the liquid at the dendrite tips
H'	average heat released per unit weight of material solidified

k	equilibrium partition ratio
ℓ	one half the plate spacing
m_L	slope of the liquidus line
N_U, N_S	total number of counts taken on the electron microprobe analyses from sample and standard, respectively
R_T	rate of advance of the dendrite tips
S', $S°$	segregation ratio at non-equilibrium solidus and room temperature, respectively
θ	time from the initiation of solidification
θ_f	solidification time
T_K	temperature, degrees Kelvin
T_L	liquidus temperature
T_S, T'_S	equilibrium solidus temperature and non-equilibrium solidus temperature, respectively
u	rate of growth of dendrite plate
x	distance from centerline of plate
X	distance from chill
X_i	position of metal interface
X_L	position of liquidus isotherm
X_{Ni}	mole per cent nickel
X_s	position of non-equilibrium solidus isotherm
X_t	position of dendrite tips measured from chill
w	relative change in the concentration gradient in the solid at the interface due to diffusion

APPENDIX B

Primary Dendrite Arm Spacings*

	1	2	3	4	5	6	7
Distance from Chill	10%Ni	15%Ni	20%Ni	26%Ni	26%Ni .1% C	26%Ni .3% C	26%Ni .4% C
1/2	47		50	72 64	90	94 97	117
1	72	64	66	110 100 99	138 144	141 136 136	214 219
1-1/2		98	97	144 135	208	177 188	
2	114 124	107	126	172 183 162 180	309 333	228 245 236	366
2-1/2	165 171	132 144	157 150	221 208	378 364	252 245	
3	194 196			282	415 415	278 294	
3-1/2		189	219	339	476 424	347 342	
4	250 231 236	206	236	368 364	474 555 578	391 387 367	551
4-1/2	260 262	225	273	460 450	617 624	406 383	
5	268			680 610 730	642 730	426	
5-1/2	298 314	287	333 332		757 737		
6	334				795 802		

* Values in left of block obtained by Area Method; on right, Linear Method. See page 56 for explanation.

Secondary Dendrite Arm Spacing

	12	14	19	4	11	10	6
Distance from Chill	10%Ni	15%Ni	20%Ni	25%Ni	25%Ni .1% C	25%Ni .3% C	25%Ni .4% C
1 in.	cells	cells	45	50	54	64 55	62 58
2 in.	88	89	78	73	80 87	80 83	82 77
4 in.	88	110	106	104	126	131	126